MATERIAL CHARACTERIZATION WITH TERAHERTZ TIME-DOMAIN SPECTROSCOPY

A THESIS SUBMITTED TO
THE GRADUATE SCHOOL OF NATURAL AND APPLIED SCIENCES
OF
MIDDLE EAST TECHNICAL UNIVERSITY

BY

DEVRİM KÖSEOĞLU

IN PARTIAL FULFILLMENT OF THE REQUIREMENTS
FOR
THE DEGREE OF DOCTOR OF PHILOSOPHY
IN
PHYSICS

JANUARY 2010

Approval of the thesis:

MATERIAL CHARACTERIZATION WITH TERAHERTZ TIME-DOMAIN SPECTROSCOPY

submitted by **DEVRİM KÖSEOĞLU** in partial fulfillment of the requirements for the degree of **Doctor of Philosophy in Physics Department, Middle East Technical University** by,

Prof. Dr. Canan Özgen _____
Dean, Graduate School of **Natural and Applied Sciences**

Prof. Dr. Sinan Bilikmen _____
Chairperson, **Physics Department**

Prof. Dr. Sinan Bilikmen _____
Supervisor, **Physics Department, METU**

Assist. Prof. Dr. Hakan Altan _____
Co-Supervisor, **Physics Department, METU**

Examining Committee Members:

Prof. Dr. Arif Demir _____
Physics Department, University of Kocaeli

Prof. Dr. Sinan Bilikmen _____
Physics Department, METU

Prof. Dr. Nizami Hasanli _____
Physics Department, METU

Prof. Dr. İbrahim Günal _____
Physics Department, METU

Assoc. Prof. Dr. Serhat Çakır _____
Physics Department, METU

Date: _____

I hereby declare that all information in this document has been obtained and presented in accordance with academic rules and ethical conduct. I also declare that, as required by these rules and conduct, I have fully cited and referenced all material and results that are not original to this work.

Name, Surname: DEVRİM KÖSEOĞLU

Signature: _____

ABSTRACT

MATERIAL CHARACTERIZATION WITH TERAHERTZ TIME-DOMAIN SPECTROSCOPY

Köseoğlu, Devrim
Ph.D., Physics Department
Supervisor: Prof. Dr. Sinan Bilikmen
Co-Supervisor: Assist. Prof. Dr. Hakan Altan

January 2010, 100 pages

Terahertz time-domain spectroscopy systems were developed and used for the anaylsis and characterization of various materials. By using ultra-fast Ti:Sapphire and Er-doped fiber lasers, terahertz time-domain spectrometers of different configurations were constructed and tested. To increase the accuracy and sensitivity of the measurements, the systems were optimized for spectroscopic analysis.

MBE grown nominally undoped epitaxial GaAs samples were used for the spectroscopic measurements. These samples were first charactrized by electrical measurements in order to check the accuracy of the terahertz time-

domain experiments. We have shown that the terahertz time-domin spectroscopic techniques provides a quick way of the determining the real (n_r) and complex (n_i) components of the refractive index of material. In addition, we have investigated the photoexcitation dynamics of these GaAs samples. We have demonstrated that direct and photoexcited terahertz time-domain measurements give an estimate of the carrier densities and both the hole and electron mobility values with good precision.

An algorithm is developed to prevent the unwanted Fabry-Perot reflections which is commonly encountered in Terahertz Spectroscopy systems. We have performed terahertz time-domain transmission measurements on ZnTe <110> crystals of various thicknesses to test the applicability of this algorithm. We have shown that the algorithm developed provides a quick way of eliminating the "etalon" reflections from the data. In addition, it is also shown that these "etalon" effects can be used for the frequency calibration of terahertz time-domain spectrometers.

Keywords: Ultra-fast lasers, Terahertz time-domain spectroscopy, Photoconductive Antennas, Optical Rectification, Electro-optic sampling, Hall Effect, van der Pauw technique, Photoexcitation, Direct-gap semiconductors, Isotropic crystals, Fabry-Perot ("etalon") effect

ÖZ

ZAMAN EKSENLİ TERAHERTZ SPEKTROSKOPİSİ İLE MATERYAL KARAKTERİZASYONU

Köseoğlu, Devrim
Doktora, Fizik Bölümü
Tez Yöneticisi: Prof. Dr. Sinan Bilikmen
Ortak Tez Yöneticisi: Yrd. Doç. Dr. Hakan Altan

Ocak 2010, 100 sayfa

Zaman eksenli terahertz spektroskopi sistemleri geliştirildi ve malzeme belirlenmesinde ve analizinde kullanıldı. Ultra-hızlı Ti:Safir ve Erbium katkılı fiber lazerler yardımıyla kurulan farklı tiplerde zaman eksenli terahertz spektrometreleri test edildi. Sistemlerin spektroskopik analiz için optimizasyonu yapılarak ölçümlerin duyarlılığı arttırldı.

Moleküler hüzme epitaksi yöntemi ile üretilen, katkılanmamış yarı-iletken GaAs örneklerinin spektroskopik ölçümleri yapıldı. Bu örnekler önce elektriksel ölçümlerle karakterize edildi ve zaman eksenli terahertz spektroskopisi sonuçlarıyla karşılaştırıldı. Böylece spektroskopic ölçümlerin duyarlılığı ve elektriksel ölçümlerle olan tutarlılığı analiz edildi. Ek olarak, laserle uyarılmış GaAs örneklerinin özellikleri çalışıldı. Bu çalışmalarda,

zaman eksenli terahertz spectroskopi yöntemlerinin çeşitli malzemelerin reel (n_r) ve kompleks (n_i) kırılma indislerinin kolayca belirlenmesine olanak sağladığı gösterildi. Bunlara ek olarak, lazerle uyarılmış ya da uyarılmamış örnekler için yapılan zaman eksenli terahertz ölçümleri ile yük yoğunluklarının, elektron ve deşik mobilitelerinin hesaplanabileceği gösterildi.

Terahertz sistemlerinde sıklıkla karşılaşılan istenmeyen Fabry-Perot yansımalarını önlemek amacıyla yazılan algoritma ile spektroskopi ölçümlerinde numerik ilerleme sağlandı. Değişik kalınlıklardaki ZnTe <110> kristallerinin zaman eksenli terahertz geçirgenlik verileri alınarak algoritma test edildi ve algoritmanın bu "etalon" etkilerinin verilerden kaldırılmasında hızlı bir yöntem olduğu gösterildi. Ayrıca bu "etalon" etkilerinin terahertz spektrometrelerin frekans kalibrasyonunda kullanılabileceği deneysel olarak gösterildi.

Anahtar Sözcükler: Zaman eksenli terahertz spektroskopisi, ultra-hızlı lazerler, Foto-iletken antenler, Optik rektifikasyon, Elektro-optik belirleme, Hall Etkisi, van der Pauw yöntemi, Işıkla uyarma, Direkt aralıklı yarı-iletkenler, İsotropik kristaller, Fabry-Perot ("etalon") etkisi

ACKNOWLEDGMENTS

I’d like to thank to my supervisor Prof. Dr. Sinan Bilikmen, co-supervisor Assist. Prof. Dr. Hakan Altan and collegue Dr. Halil Berberoğlu for their guidance, advice, criticism and encouragements.

I’d like to thank to the examining committee members for their suggestions and comments.

This study was supported by TÜBİTAK - TBAG (1001 Project No. 107T742).

TABLE OF CONTENTS

ABSTRACT …….....iv
ÖZ …….....vi
ACKNOWLEDGMENTS ……...viii
TABLE OF CONTENTS …….....ix
LIST OF FIGURES ……...xi
LIST OF SYMBOLS ……..xiv
LIST OF TABLES ……..xv
CHAPTERS
1. INTRODUCTION ……..1
2. TERAHERTZ TIME-DOMAIN SPECTROSCOPY ……...….4
2.1 Introduction ……...4
2.2 Femtosecond Laser Pulses ……6
2.2.1 Ti: Sapphire Lasers ……....7
2.2.2 Erbium-doped Fiber Lasers ……12
2.3 Basics of THz Generation and Detection ……14
2.3.1 THz Pulse Generation Methods ……..14
2.3.1.1 Photoconductive Antennas ……...14
2.3.1.2 Optical Rectification ……23
2.3.2 THz Pulse Detection Methods ……28
2.3.2.1 Photoconductive Antennas ……...28
2.3.2.2 Electro-optic Sampling ……..…29
2.4 Typical THz-TDS configurations ……30
2.4.1 THz-TDS system based on photoconductive antenna generation and photoconductive antenna detection ……30
2.4.2 THz-TDS system based on photoconductive antenna generation and electro-optical detection ……33

2.4.3 THz-TDS system based on optical rectification and electro-optic sampling via difference frequency mixing .35
2.5 Terahertz Time-Domain Spectral Analysis ……..…39
3. ELECTRICAL CHARACTERIZATION OF MBE GROWN EPITAXIAL GaAs ……...42
3.1 Introduction ……42
3.2 The van der Pauw Technique ……..42
3.3 The Hall Effect ……...46
3.4 Experiment ……..48
3.5 Results ……50
3.6 Discussion……51
4. TERAHERTZ PROBE STUDIES OF MBE GROWN EPITAXIAL GaAs ……54
4.1 Introduction ……54
4.2 Drude Model ……55
4.3 Experiment ……..58
4.4 Analysis ……...62
4.5 Discussion ……...65
5. NUMERICAL IMPROVEMENT OF TERAHERTZ TIME-DOMAIN SPECTROSCOPIC MEASUREMENTS ……67
5.1 Introduction ……67
5.2 Fabry-Perot Effect ……...……67
5.3 The Algorithm ……69
5.4 Experiment ……..72
5.5 Frequency Calibration Test using the Etalon Model ……...78
5.6 Discussion ……...80
6. CONCLUSION ……....81
REFERENCES ……85
APPENDICES
A. NUMERICAL IMPROVEMENT SOFTWARE...……...……93
B. PREPULSE EFFECTS IN THz-TDS ……..97

VITA ……100

LIST OF FIGURES

FIGURES

Fig.2.1. The THz band and the THz absorption spectra ...……..…5
Fig.2.2. The photo of the Femtosource oscillator ……...8
Fig.2.3. The Femtosource Ti: Sapphire laser used in this thesis ……8
Fig.2.4. Femtolasers Acquisition Tool used for laser output measurements …10
Fig.2.5. Determination of centre wavelength ……...11
Fig.2.6. Fringe pattern ……..12
Fig.2.7. Er-doped fiber laser amplifier system ……13
Fig.2.8. An electric dipole ……16
Fig.2.9. The current segment of the oscillating dipole ……18
Fig.2.10. THz radiation from PCA ……...20
Fig.2.11. Photoconductive antenna ……..22
Fig.2.12. Terahertz Photoconductive Antenna ……..…31
Fig.2.13. THz-TDS system based on PCAs ……31
Fig.2.14. The time-domain profile for air of the THz-TDS using photoconductive antenna generation and electro-optic sampling detection ……...32
Fig.2.15. The frequency spectrum for air of the THz-TDS using PCA generation and PCA detection ……..32
Fig.2.16. THz-TDS based on antenna generation and electro-optic sampling .33
Fig.2.17. The time-domain profile for air of the THz-TDS using photoconductive antenna generation and electro-optic sampling detection ……...34
Fig.2.18. The frequency spectrum for air of the THz-TDS using photoconductive antenna generation and electro-optic sampling detection ……...34
Fig.2.19. THz-TDS based on optical rectification and electro-optic sampling 36
Fig.2.20. THz time domain pulse profile produced by 1 mm ZnTe <110> ….37

Fig.2.21. THz-pulse FFT profile produced by 1 mm ZnTe <110> ……..37
Fig.2.22. THz time domain pulse profile produced by 2 mm ZnTe <110> ….38
Fig.2.23. THz-pulse FFT profile produced by 2 mm ZnTe <110> ……..38
Fig.3.1. Typical symmetrical sample geometries (a. disk, b. cloverleaf, c. square or rectangle with contacts at the corners, d. square or rectangle with contacts at the edges) for van der Pauw and Hall effect measurements. ……..……38
Fig.3.2. Determination of R_A and R_B ……...44
Fig.3.3. The Hall effect ……47
Fig.3.4. Setup for Hall effect and van der Pauw measurements ……..49
Fig.3.5. The switch box used to change the contact points ……..50
Fig.3.6. The GaAs structure ……52
Fig.4.1: THz spectroscopy system for the probe measurements 59
Fig.4.2: THz-TDS scan of the direct spectroscopy of GaAs compared with air 60
Fig.4.3: FFT of the direct spectroscopy of GaAs compared with air ……...60
Fig.4.4: THz-TDS of Time-Domain scan of the photoexcited spectroscopy ...61
Fig.4.5: FFT of the photoexcited spectroscopy ……61
Fig.4.6: The real part of the refractive index obtained by direct and photoexcited THz spectroscopy ……...63
Fig.4.7: The conductivities obtained by direct and photoexcited THz spectroscopy with their Drude fits ……....64
Fig.5.1. The THz time-domain data for the 1 mm ZnTe data ……..67
Fig.5.2. The THz FFT transformed data for the 1 mm ZnTe data …...……68
Fig.5.3. An example of the determination of etalon reflections and the implementation of the removal procedure ……70
Fig.5.4. The THz time-domain spectrum after the implementation of the algorithm ……..…..71
Fig.5.5. THz spectroscopy system for the transmission measurements …...…72
Fig.5.6. THz time-domain transmission data for the reference and 1.0 mm, 1.5 mm, 2.0 mm thick <110> ZnTe crystals ……73

Fig.5.7. THz time-domain spectroscopic data for (a) reference and (b) 1 mm (c) 1.5 mm (d) 2 mm thick ZnTe <110> crystals sample ……..…74
Fig.5.8. Fourier Transforms for (a) reference and (b) 1 mm (c) 1.5mm (d) 2 mm thick ZnTe <110> crystals with and without algorithm ...…75
Fig.5.9. Absorption spectrum of (a) 1 mm (b) 1.5 mm (c) 2 mm thick ZnTe <110> crystal samples with and without algorithm …….76
Fig.5.10. Transmission spectrum on 1 mm thick ZnTe and the “etalon” model ……78

LIST OF SYMBOLS

$\mathbf{E}(t)$	Electric field
$\mathbf{B}(t)$	Magnetic field
$\mathbf{J}(t)$	Current density
$\mathbf{p}(t)$	Dipole moment
$\Phi(\mathbf{r}, t)$	Electric potential
$\mathbf{A}(\mathbf{r},t)$	Vector potential
$P(t)$	Electric polarization
$\chi_e(\omega)$	Electric susceptibility
ε_0	Permittivity of free space
$n(\omega)$	Refractive index
$\varepsilon(\omega)$	Dielectric function
$\sigma(\omega)$	Conductivity
R_s	Sheet resistance
ρ	Resistivity
V_H	Hall voltage
n_s	Sheet charge density
n	Charge carrier density
μ	Mobility
R_H	Hall coefficient
τ	Relaxation time
α	Absoption coefficient
ν_c	Collision frequency
ω_p	Plasma frequency
m_p^*	Effective mass of holes
m_n^*	Effective mass of electrons
N	Number density

LIST OF TABLES

TABLES

Table 3.1. The experimental results for MBE grown epitaxial GaAs ……..51

CHAPTER 1

INTRODUCTION

The unexplored terahertz (THz) region of electromagnetic spectrum is taking much interest due to the lack of efficient methods to generate and detect THz radiation. It is a developing area which lies in between optics and electronics. From the optics side, terahertz research provides information on the vibrational and rotational modes of atoms and molecules in materials. While the Terahertz time-domain spectroscopic techniques are generally used for the determination of the optical properties and the study of the dynamics of semiconductors, the terahertz imaging techniques have gained much attention because of their potential use in imaging, remote sensing and homeland security [1]. From the electronics side, the high sensitivity generation and detection devices and their implantation into this area of research and technology combines the field of microwave engineering and optical engineering into photonics. What makes this method unique is that the Terahertz time-domain spectroscopy systems are capable of coherent generation and detection of THz radiation, so that the amplitude and the phase of the THz beam are measured simultaneously.

In THz time-domain spectroscopy, the amplitude and phase of the THz radiation is measured coherently as a function of time. The spectrum is obtained by a Fourier transform of the time domain data. With this information, it is possible to do spectroscopic analysis and to calculate the complex dielectric function of materials without solving the Kramers-Kronig relations. So, it is a practical tool for material characterizations.

To generate and detect THz radiation is a very difficult and complicated task. THz researchers generally construct their own systems, since the market for THz technology is almost unavailable. The construction or implementation of ultra-fast lasers requires high skill and technological understanding. The research in terahertz time-domain spectroscopy is intimately related to the developments in the ultra-fast laser design. For this reason, the invention of low-cost, compact, and turn-key femtosecond lasers will help the THz spectroscopists to develop commercially available systems.

The implementation of photoconductive antennas [2 - 5], optical rectification [6 - 13], and electro-optic sampling [14 - 16] into the terahertz research enhanced the terahertz studies and started the science of terahertz optoelectronics. Today, the terahertz optoelectronics is applied in the areas of spectroscopy [17 - 19], imaging [20 - 22], microscopy [23], tomography [24, 25], biology [26], and defense [27, 28].

The objective of this thesis is to investigate various characteristics of different terahertz time-domain spectroscopy systems and study their use in material characterization. In this study, we constructed terahertz time-domain spectrometers based on the methods mentioned above to check their properties and limitations. We have optimized these systems for material characterization.

In the second chapter, the systems we have developed were described together with the basics of terahertz time-domain spectroscopy.

In the third chapter, the electrical characterization of nominally undoped expitaxial GaAs samples were explained.

In the fourth chapter, the terahertz time-domain studies of these samples were presented.

In terahertz time-domain spectroscopic measurement, there exists additional pulses after the main peak due to Fabry-Perot effect [29]. We have developed an algorithm which was given in the appendix to remove these “etalon” oscillations by using the method by M. Naftaly and R.E. Miles [30] and applied these to the transmission analysis of ZnTe <110> crystals of different thicknesses. We have also used this “etalon model” [29 - 31] to remove the Fabry-Perot effect and to check the calibration of our spectrometers. These studies were presented in the fifth chapter. The conclusion chapter summarizes the overall studies done in this thesis.

CHAPTER 2

TERAHERTZ TIME-DOMAIN SPECTROSCOPY

2.1. Introduction

In this chapter, the commonly used Terahertz (THz) radiation generation and detection methods will be covered briefly. The basics of THz time-domain spectroscopy systems will be described together with the ultra-fast lasers used in this thesis. Later, the THz spectral analysis technique is presented.

The definition of "THz gap" generally covers the region from 300 GHz (λ = 1 mm) to 10 THz (λ = 30 μm). It lies between the microwave and the far-infrared part of the electromagnetic spectrum (see Figure 2.1). Therefore, it is a transition region from electronics to the optics. The photon energy corresponding to 1 THz (10^{12} Hz) is 4.1 meV (33.33 cm^{-1}).

The unexplored "THz gap" has attracted a lot of attention in terms of scientific and technological purposes in the last decade. With the development of compact and low-cost femtosecond laser sources working at room temperature, the research on the area of terahertz optoelectronics has enhanced potential application areas such as spectroscopy, imaging, as well as chemical and biological sensing.

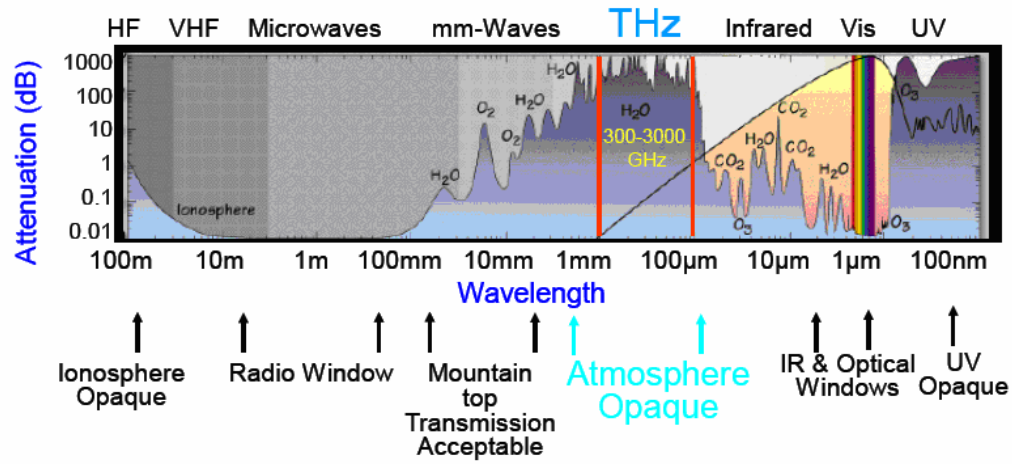

(*Chart reference: http://www.envisat.esa.int/instruments/mipas/descr/concept.html#introduction*)

Fig.2.1. The THz band and the THz absorption spectra

Among the commonly used applications of THz technologies, spectroscopic methods allow a material's far-infrared optical properties to be determined as a function of frequency. This information can provide knowledge on the material characteristics for a wide range of applications. There are generally three different THz spectroscopy techniques: These are Terahertz Time-Domain Spectroscopy (THz-TDS), Time-Resolved Terahertz Spectroscopy (TRTS), and Terahertz Emission Spectroscopy (TES). THz-TDS is used to investigate the static properties of the material. On the other hand, TRTS is used for the analysis of the dynamic properties. In the TES, the material under study itself emits THz radiation, from the detected radiation, the emission characteristics of the material is determined.

THz systems (THz-TDS and TRTS) use very short pulses (of the order of femtoseconds) of broadband THz radiation, which are typically generated using ultra-fast laser pulses. Ultra-fast lasers enable the use of time-gating methods to detect the electric field of the THz pulses as a function of time. In a typical THz spectroscopy system, femtosecond pulses are directed to a generation medium to be used for excitation. The generation medium produces electromagnetic pulses whose electric field depends on the intensity and width

of the envelope of the femtosecond pulses. The transmitted THz electric field is then measured coherently, which provides both amplitude and time-resolved phase information.

2.2. Femtosecond Laser Pulses

The term "*ultra-fast*" is generally used for pulses less than picoseconds. To generate picosecond pulses, a broadband laser has to be used, since the duration of an optical pulse is related to the bandwidth of the source via the Heisenberg uncertainty relation.

$$\Delta\upsilon \cdot \Delta\tau \geq 1 \tag{2.1}$$

where $\Delta\nu$ is the laser bandwidth and $\Delta\tau$ is the duration of the laser pulse. Numerically, for a picosecond pulse, a laser bandwidth of at least a THz is needed. This bandwidth is higher than ordinary lasers, such as Nd:YAG, Nd:Glass, Excimer (XeCl, ArF, KrF), and gas atom or ion (He-Ne) lasers. So, broad bandwidth sources such as Ti:Sapphire lasers, Erbium-doped fiber lasers, high-pressure CO_2 lasers, or Dye lasers can be used to generate ultra-fast pulses [32 - 35].

Frequency doubling and optical parametric oscillation techniques are applied to get output from the infrared to the ultraviolet range in addition to the mode-locking principles. These nonlinear techniques are commonly used in ultra-fast lasers. In this thesis, mode-locked Ti^{+3}:Sapphire and Er^{+3}-doped fiber lasers were used together with the optical elements, auto-correlators and pumping lasers.

2.2.1. Ti: Sapphire lasers

Among the tunable solid state lasers, Ti:Sapphire is probably the most popular and novel one which is based on the active medium consisting of Ti^{+3} ions (typically 0.1 %) in the lattice of Al_2O_3 crystal. Ti:Sapphire crystal absorbs the output of a pump laser which is emitting in the green region of the electromagnetic spectrum and produces wavelengths between 720 nm to 880 nm. So, they produce enough broad bandwidth for the generation of sub-picosecond ultra-fast pulses. However, the complexity of the design, delicate nonlinear optical elements, and auto-correlators, in addition to the requirement of a very good quality pump laser, make these lasers quite complex and expensive. Ti:Sapphire lasers are sensitive to vibrations and temperature changes, so the user has to align the optics regularly to achieve the best possible performance.

Ti:Sapphire lasers can produce very short femtosecond pulses in mode-locked operation which can be used especially for characterization of materials and investigation of the rotational and vibrational dynamics of atoms in a molecule.

The Ti:Sapphire lasers generally employ a diode-pumped Nd:YVO_4 solid state laser. The frequency doubled 532 nm beam is directed into the resonator to pump the Ti^{+3}:Al_2O_3 crystal. The optical length of the resonator is around 3.75 meters, so the pulses are produced at a repetition of 80 MHz. The Ti:Sapphire laser used in this thesis is shown in Figure 2.2 and 2.3 [36].

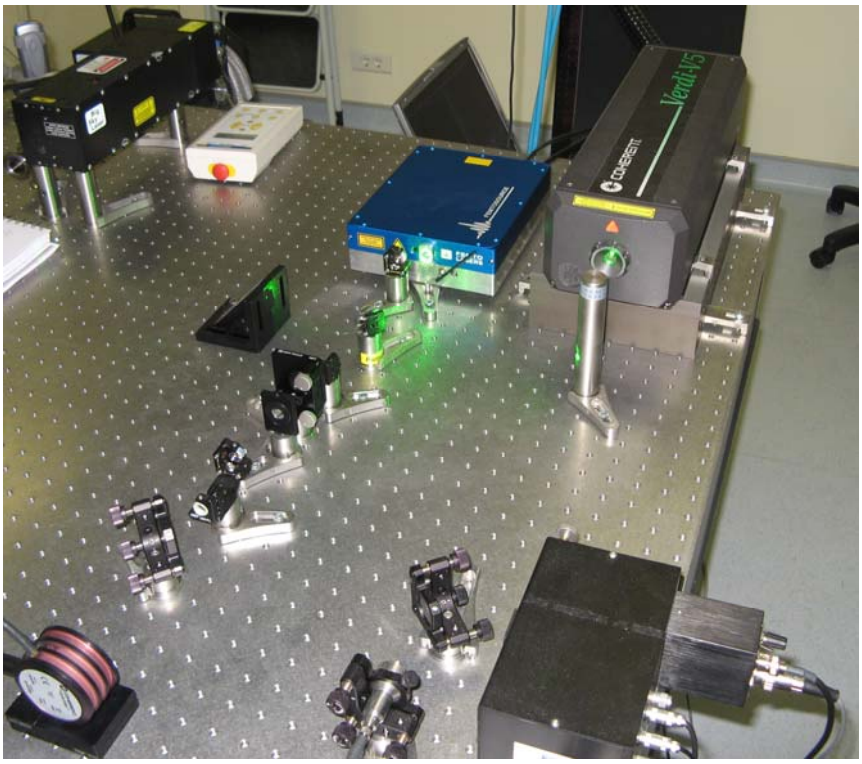

Fig.2.2. The photo of the Femtosource oscillator

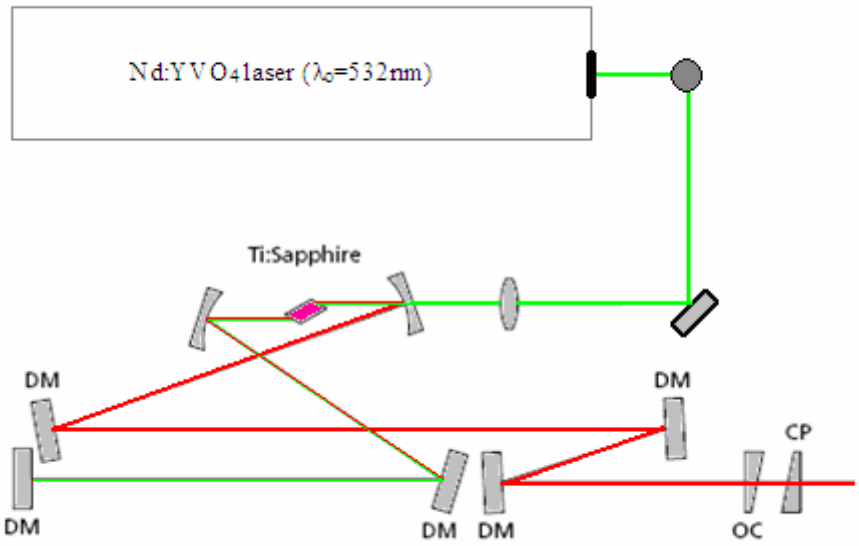

Fig.2.3. The Femtosource Ti: Sapphire laser used in this thesis

The femtosecond Ti:Sapphire laser used in the terahertz time-domain spectroscopy systems constructed in this study consists of the following components:

I. Pump laser - Coherent Verdi (V5) Nd:YVO_4 laser (λ_o=532nm)
II. Compact Laser Head - Femtosource
III. Periscope
IV. Optomechanical units
V. Optics
VI. Extra-cavity Dispersion Control
VII. Solid State Chiller (Thermotek)
VIII. Dispersion Minimized Autocorrelator (Femtometer)

The pump-laser is a single frequency solid-state laser producing continuous waves at 532 nm. It is capable of producing laser powers up to 5 W. The mode of the pump beam is TEM_{00} which is the fundamental mode of operation. The pump beam is vertically polarized (s-polarization) while the compact laser head requires horizontally polarized (p-polarization) pump beam. The periscope which is used for changing the height of the pump beam also changes its polarization to horizontal polarization. The out beam of the periscope is directed to the compact laser head by using steering mirrors. The laser head contains a focusing lens for the pump beam, dicroic dispersive focusing mirrors for resonator beam, and a highly doped Ti:Sapphire crystal. There are three micrometer screws for optimization of the compact laser head. They are used for the adjustment of the position of the Ti:Sapphire crystal and the stability range. The end mirror of the compact laser head is placed on a translational stage for active mode-locking.

The pump laser and the compact laser head is cooled by using a solid state cooling unit which stabilized the heat of the Ti:Sapphire crystal around 19 ^oC. The thermal stability of the compact laser crystal is of crucial importance for

the stability of the laser beam and for the maintenance of both the pump-laser and the compact laser head. [36, 37].

The characterization of the output mode-locked pulses in the time-domain is analyzed by using an autocorrelator which is connected to a computer utilizing data acquisition software. The autocorrelator has the following parts:

I. BBO frequency doubling crystal (less than 25µm thick)
II. Dielectric broad-band beam-splitter for p-polarized light
III. Silver coated reflective optics
IV. Piezo-driven scan stage (full scan-range is higher than 500 fs)
V. Frequency generator (0.2 Hz to 20 Hz)
VI. Low dispersion over-coated silver steering optics
VII. Broad-band beam splitters
VIII. MHz detection module utilizing a photomultiplier with integrated high voltage supply and sensitivity adjustment
IX. Data acquisition software

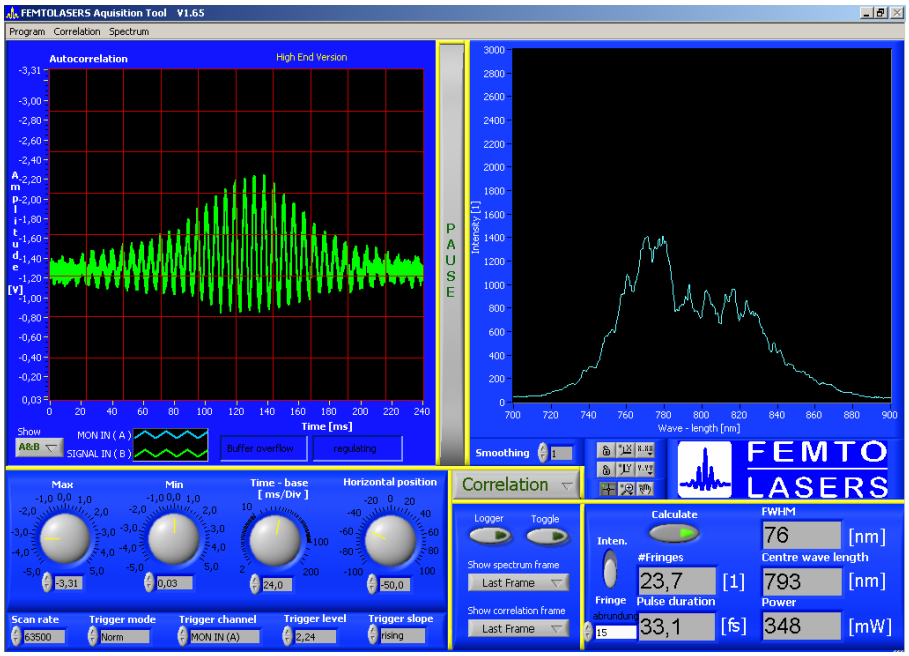

Figure 2.4. Femtolasers Acquisition Tool used for laser output measurements

The autocorrelator system coupled with a spectrometer is capable of measuring the full-width-at-half-maximum (FWHM) and number of fringes. A screenshot of the Femtolasers Data Acquisition system is shown in Figure 2.4 [37]. From these values the centre wavelength (λ_o) and the pulse duration is calculated.

From the spectrum, the FWHM is determined and λ_o is found. From λ_o, the fringe spacing can be estimated by

$$\Delta\tau = \frac{\lambda_0}{c} \ . \tag{2.2}$$

The full-width-at-half-maximum (FWHM) and the centre wavelength (λ_o) is illustrated in Figure 2.5. For this data, λ_o is found to be 793 nm and the FWHM is 76 nm.

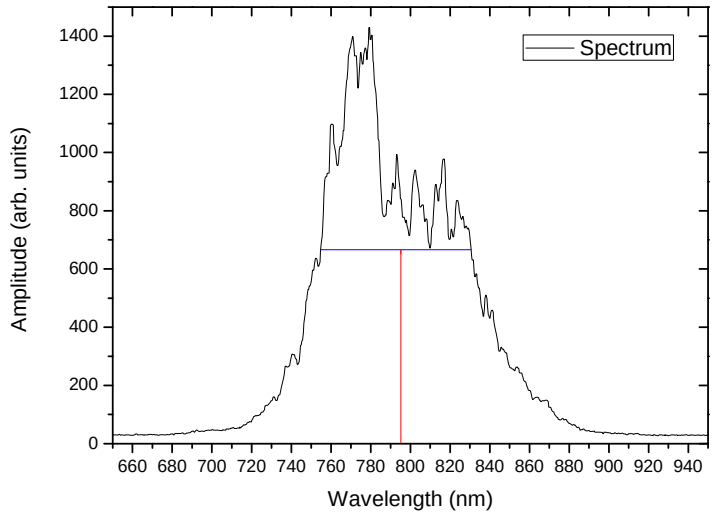

Fig.2.5. Determination of centre wavelength

The total number of fringes can be estimated by counting the number of fringes above the 50% line by linear interpolation to determine the percentage of the fringe-period at the 50% line as depicted in Figure 2.6 [37, 42, 43].

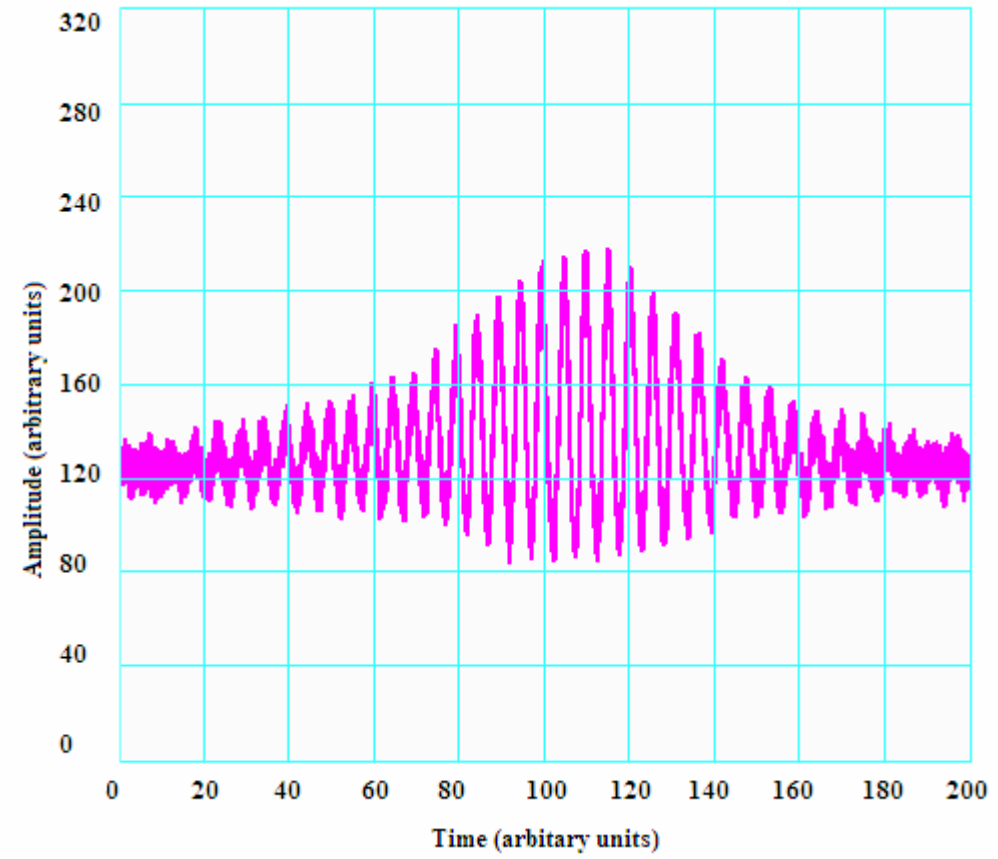

Fig.2.6. Fringe pattern

The deconvolution factor, B, is determined by assuming a sech^2 pulse shape. The pulse duration at FWHM, then, is calculated by [37, 42, 43]:

$$t_P = \frac{N \times \Delta\tau}{B} \quad . \tag{2.3}$$

The femtosecond laser system uses chirped multi-layer dielectric mirrors for broadband intra-cavity group-delay-dispersion control and better optical time resolution [38 - 41]. The system also has a mirror-dispersion-control which utilizes low-dispersion quarter wave mirrors to couple the laser beam the resonator and mode-locked pulse out of the resonator. The overall system is optimized for generation of almost bandwidth limited optical pulses of sub-30 ps in duration.

2.2.2. Er-doped fiber lasers

In the last decade, the progress on the fiber laser technology has opened the way to obtain ultra-fast pulses from compact, inexpensive, and turn-key equipment. The Er^{+}-doped fiber lasers are probably the most popular and novel one which is based on the active medium consisting of Er^{+3} ions in the fiber, since they have potential use in optical communications, sensors, and measurement science. However, they produce less power and longer pulses when compared with the Ti:Sapphire systems.

Mode-locked Erbium doped fiber lasers has a fundamental output at 1560 nm. Their output power is generally increased by using a fiber-optic stretched pulse amplifier system. The gain in output power with the use of a fiber optic stretch pulse amplifier system enables efficient frequency doubling. Typical Er^{+3}-doped fiber laser is shown in Figure 2.7. In this system, Er^{+3}-doped fibers are pumped with high efficiency 980 nm diodes capable of providing in excess of 500 mW of average power [44, 45].

Fig.2.7. Er-doped fiber laser amplifier system

Using doped optical fibers leads Raman scattering and produces 1560 nm wavelengths. After the mode-locking process, the 1560 nm laser output is frequency doubled by using a periodically poled $LiNbO_3$ crystal to generate the second harmonic at 780 nm with 30 % conversion efficiency to produce output power typically at around 100 mW.

2.3. Basics of Terahertz Pulse Generation and Detection

Auston *et al.* [9 - 11], accomplished the first generation and detection of picosecond electromagnetic pulses with a structure which is known today as the Auston switch. The coherent detection of these picosecond pulses was the corner stone of the field THz time-domain spectroscopy. Later, Auston *et al.* [12], also introduced the non-linear techniques of generation which are based on the second order non-linear effects in wide band-gap crystals. These methods have lead to generation of wideband THz pulses of up to 70 THz [46].

2.3.1. THz Pulse Generation Methods

THz radiation can be generated in many ways. However, in THz Time-Domain Spectroscopy, THz pulses are generally produced either by photoconductive antennas or optical rectification techniques. In this thesis, both of these methods were used.

2.3.1.1. Photoconductive Antennas

Antenna is a device for receiving and transmitting electromagnetic waves. It is an interface between free space and electronic components. According to the reciprocity theorem, antennas show identical properties in receiving and transmitting modes [47].

THz generation with photoconductive antennas is based on the rapid change in conductivity of a fast response material with the optical excitation by ultra-fast laser pulses. The motion of charge carriers produced in the depletion region of a semiconductor surface triggered by an ultra-short laser pulse provides a convenient source of coherent electromagnetic radiation in the THz spectral region.

In order to create electron-hole pairs in the antenna, the photons of the ultra-fast excitation laser used in the generation process is to be higher than the band gap energy of the semiconductor used in the antenna. The laser light is generally focused on to the dipole gap of the antenna. The optically excited electron-hole pairs are created between the conductor lines of the antenna. As the carriers accelerate under an external bias (E-field) THz radiation is emitted [47]. In the near field the THz electric field follows the envelope of the laser pulse [47], since the charge carriers are accelerated only when the laser pulse is present within the gap of the antenna. On the other hand, in the far field, the THz electric field is related to the transient photocurrent as [47]

$$E(t) \propto \frac{\partial J(t)}{\partial t} \tag{2.4}$$

This relation can be derived by approximating the antenna structure as an Hertzian electric dipole (Figure 2.8) [48]. Here we shall give a brief derivation of the relation between the terahertz electric field and the transient photocurrent density based on the electric dipole radiation model. In this model, we shall start with the field equations for far field radiation from an electric dipole. We shall use this model to describe the THz radiation from a narrow gap Hertzian photoconductive antenna.

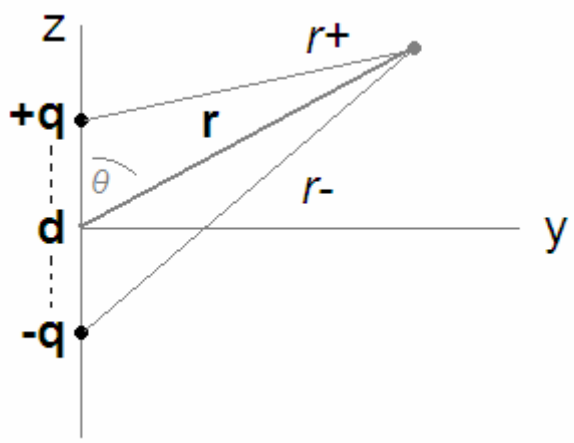

Fig.2.8. An electric dipole

We assume the dipole is made of two very small metal spheres which are connected to each other by a very thin and perfectly conducting wire. The distance between the charged spheres is *d*, and at time *t* = 0, the charge of the upper sphere is $+q_o$ and that of the lower one is $-q_0$. The value of the dipole moment at $t = 0$ is

$$p_0 = q_0 d \ . \tag{2.5}$$

If the charges are driven up and down through the wire, from one sphere to the other with an angular frequency (ω), the system of two spheres can be described as an oscillating dipole:

$$\mathbf{p}(t) = p_o \cos(\omega t)\hat{\mathbf{z}} \tag{2.6}$$

The retarded potential for this configuration is written as

$$\Phi(\mathbf{r},t)=\frac{1}{4\pi\pi_0}\left\{\frac{q_0\cos\left[\omega\left(t-\frac{r_+}{c}\right)\right]}{r_+}-\frac{q_0\cos\left[\omega\left(t-\frac{r_-}{c}\right)\right]}{r_-}\right\} \tag{2.7}$$

where r_+ and r_- are given by the trigonometric equation

$$r_\pm=\sqrt{r^2\mp rd\cos\theta+\left(d/2\right)^2}\ . \tag{2.8}$$

For the field far away from the dipole where the wavelength (λ) is much smaller than the distance (r) from the dipole, the radiation zone approximation

$$r\rangle\rangle\frac{c}{\omega} \tag{2.9}$$

can be used. So, in the radiation zone, the potential can be approximated by

$$\Phi(r,\theta,t)=-\frac{p_o\omega}{4\pi\pi_0 c}\left(\frac{\cos\theta}{r}\right)\sin\left[\omega(t-\frac{r}{c})\right] \tag{2.10}$$

The current flowing up and down with the angular frequency (ω) through the wire is given by

$$\mathbf{I}(t)=\frac{dq}{dt}\hat{\mathbf{z}}=-q_0\omega\sin(\omega t)\hat{\mathbf{z}} \tag{2.11}$$

The vector potential for the configuration shown in Figure 2.9 becomes

$$\mathbf{A}(r,t)=\frac{\mu_0}{4\pi}\int_{-d/2}^{d/2}\frac{-q_0\omega\sin\left[\omega(t-\Re)\right]\hat{\mathbf{z}}}{\Re}dz \tag{2.12}$$

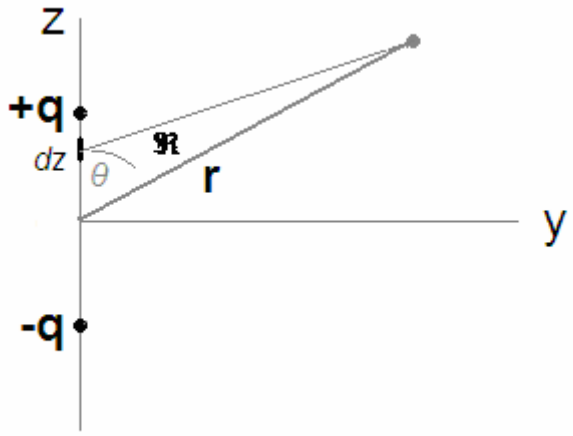

Fig.2.9. The current segment of the oscillating dipole

The vector potential can be written in polar coordinates as

$$\mathbf{A}(r,\theta,t) = -\frac{\mu_0 p_0 \omega}{4\pi r}\sin\left[\omega(t-\frac{r}{c})\right]\hat{\mathbf{z}} \tag{2.12}$$

The fields are calculated from the potentials as

$$\nabla\Phi = \frac{\partial\Phi}{\partial r}\hat{\mathbf{r}} + \frac{1}{r}\frac{\partial\Phi}{\partial\theta}\hat{\boldsymbol{\theta}} \tag{2.13}$$

From the $\Phi(r,\theta,t)$, the $\nabla\Phi$ is calculated

$$\nabla\Phi = -\frac{p_0\omega}{4\pi\pi_0 c}\left\{\cos\theta\left(-\frac{1}{r^2}\sin\left[\omega(t-\frac{r}{c})\right] - \frac{\omega}{rc}\cos\left[\omega(t-\frac{r}{c})\right]\right)\hat{\mathbf{r}} - \frac{\sin\theta}{r^2}\sin\left[\omega(t-\frac{r}{c})\right]\hat{\boldsymbol{\theta}}\right\}$$

(2.14)

This equation can be approximated for the far-field radiation zone as

$$\nabla\Phi \cong \frac{p_0\omega^2}{4\pi\pi_0 c^2}\left(\frac{\cos\theta}{r}\right)\cos\left[\omega(t-\frac{r}{c})\right]\hat{\mathbf{r}} \tag{2.15}$$

The vector potential in the radiation zone can be written as

$$\frac{\partial \mathbf{A}}{\partial t} = -\frac{\mu_0 p_0 \omega^2}{4\pi\pi}\cos\left[\omega(t-\frac{r}{c})\right](\cos\theta\,\hat{\mathbf{r}} - \sin\theta\,\hat{\boldsymbol{\theta}}) \tag{2.16}$$

So, the electric field is

$$\mathbf{E} = -\nabla\Phi - \frac{\partial \mathbf{A}}{\partial t} = -\frac{\mu_0 p_0 \omega^2}{4\pi}(\frac{\sin\theta}{r})\cos\left[\omega(t-\frac{r}{c})\right]\hat{\boldsymbol{\theta}} \tag{2.17}$$

The electric dipole radiation model can be used to explain the terahertz radiation generation mechanism in a photoconductive antenna, since the size of a Hertzian photoconductive antenna is much smaller than the wavelengths of the emitted terahertz radiation [48]. So, the terahertz electric field in free space for the radiation zone, as shown in Figure 2.7, can be written as

$$\mathbf{E}_{THz}(t) = \frac{\mu_0}{4\pi}\frac{\sin\theta}{r}\frac{d^2}{dt_R^2}[p(t_R)]\hat{\boldsymbol{\theta}} \tag{2.18}$$

where $p(t_R)$ is the value of the dipole moment of the source at the retarded time $t_R = t - \frac{r}{c}$.

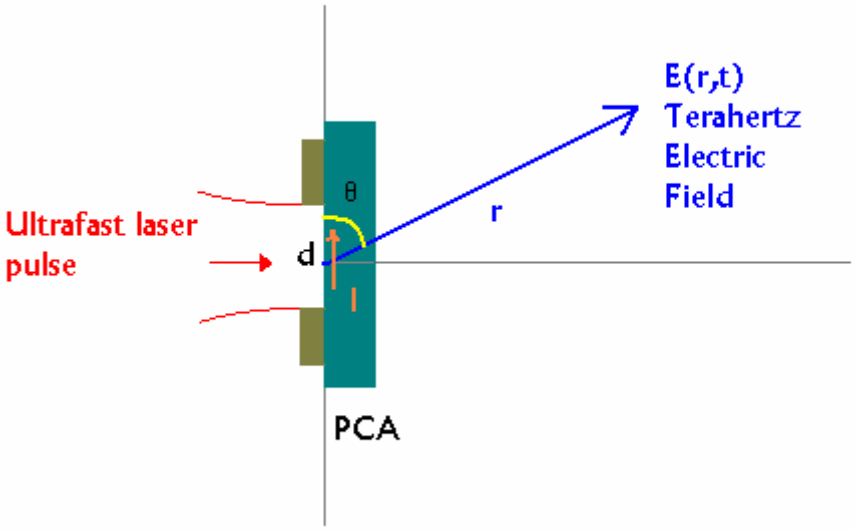

Fig.2.10. THz radiation from PCA

The time derivative of the dipole moment can be expressed in terms of the transient photocurrent density, $\mathbf{J}(\mathrm{r},t)$, which is related to the charge density through the continuity equation:

$$\nabla \cdot \mathbf{J} + \frac{\partial \rho}{\partial t} = 0 \ . \tag{2.19}$$

The time derivative of the dipole moment is

$$\begin{aligned} \frac{d\mathbf{p}(t)}{dt} &= \frac{d}{dt}\int \rho(\mathbf{r}',t)\mathbf{r}'d^3\mathbf{r}' \\ &= \int \mathbf{r}' \frac{\partial \rho(\mathbf{r}',t)}{\partial t} d^3\mathbf{r}' \end{aligned} \tag{2.20}$$

Then, the time derivative of the current density is written in terms of the current density as

$$\frac{d\mathbf{p}(t)}{dt} = -\int \mathbf{r}'\nabla\cdot\mathbf{J}(\mathbf{r}',t)d^3\mathbf{r}' = \int \mathbf{J}(\mathbf{r}',t)d^3\mathbf{r}' \tag{2.21}$$

If the spot size diameter of the ultra-fast laser beam is equal to d and I_{PCA} is the transient photocurrent density induced in the antenna

$$\frac{dp(t)}{dt} = \int_{-d/2}^{d/2} I_{PCA}(z',t)dz' = I_{PCA}(t)\times d \tag{2.22}$$

So, the terahertz electric field can be written as [48]

$$\mathbf{E}_{THz}(t) = \frac{\mu_0 d}{4\pi}\frac{\sin\theta}{r}\frac{d}{dt_R}[I_{PCA}(t_R)]\hat{\boldsymbol{\theta}} \tag{2.23}$$

Therefore, the terahertz electric field is found to be proportional to the current density through the relation

$$E(t) \propto \frac{\partial J(t)}{\partial t}\ , \tag{2.24}$$

since the volume current density is equal to

$$\mathbf{J} = \frac{d\mathbf{I}_{PCA}}{da_\perp} \tag{2.25}$$

where $da_\perp$ is the infinitesimal cross section perpendicular to the current flow. The time derivative of the photocurrent is very high, since the duration of the exciting laser pulse is very short. The duration of the emitted THz pulse is of

the order of picoseconds. This emission is broadband and in a Hertzian dipole radiation pattern [48]. So, it should be collimated by focusing elements in THz spectroscopy systems.

It is also possible to generate THz fields without an external bias, but this results in quite low field strengths [47]. It is also reported that application of external magnetic field may improve the quality and strength of the THz emission in certain materials. On the other hand, it is also noted that focusing the ultra-fast laser beam closer to one of the electrodes also enhances the emission strength of the photoconductive antenna [47].

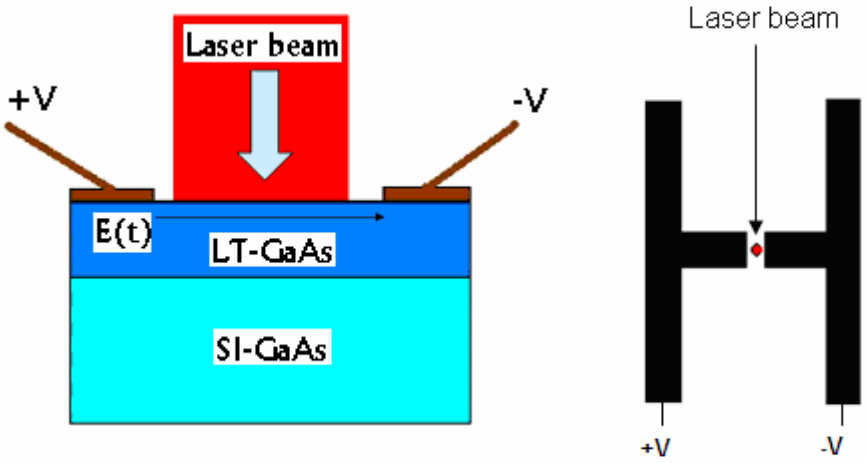

Fig.2.11. Photoconductive antenna

Highly resistive semiconductors, such as Lt-GaAs are used in the production of photoconductive antennas, since when the laser pulse penetrates the semiconductor, the creation of charge carriers lowers the resistance of the semiconductor. The response of the semiconductor should be fast enough so that between the laser pulses, the semiconductor can turn back to its original state. In this sense, the antenna acts as a switch that allows the bias field to accelerate the charge carriers rapidly in a single laser pulse duration, then the carriers recombine and the current between the dipoles returns to its original value. For this reason, photoconductive antennas are also called

photoconductive switches [48]. In order to lower the noise and increase the sensitivity, the bias field is modulated by a function generator, which is used subsequently in lock-in measurement techniques.

2.3.1.2. Optical Rectification

Optical rectification is a non-linear optical effect that produces a polarization in a non-linear medium by an intense optical beam. Typically, THz radiation is generated by optical rectification while an intense femtosecond laser beam propagates through the generation crystal. This laser pulse induces a beating polarization because of the spectral width of the laser pulse. This time dependent dielectric polarization produces pulsed radiation. This method has been used for producing broadband THz radiation [46].

Here we shall try to physically describe the method of optical rectification in a medium. High power laser beams are capable of increasing the oscillation amplitudes of the electrons in a medium. This may result in nonlinear electron motion. These nonlinear effects can be modeled by adding a small nonlinear perturbation to the linear system, which can be assumed to be well described by a harmonic oscillator model [48].

In the linear system, the oscillation amplitudes are assumed to be small enough that the optical response of the medium depends on the motion of the electric dipoles. The dipole moments of electrons are related to the amplitude of the applied field. If the effects of the magnetic field is negligible, the equation of motion of electrons can be written by applying the Lorentz model. In this model, the electrons are considered as simple harmonic oscillators with very small amplitudes. Under a monochromatic electric field

$$E(t) = E_0 e^{-i\omega t} \tag{2.26}$$

of polarization along the *x*-axis and of angular frequency ω, the equation of motion for an electron is expressed as

$$\frac{d^2x}{dt^2} + \gamma\frac{dx}{dt} + \omega_0^2 x = \frac{e}{m}E(t) \tag{2.27}$$

where γ is the dissipation constant and ω_0 is the resonance frequency. The solution of this differential equation is

$$x(t) = \left(\frac{e}{m}\frac{E_0}{\omega_0^2 - \omega^2 - i\omega\gamma}\right)e^{-i\omega t} \tag{2.28}$$

which can be rewritten as

$$x(t) = x_0 e^{-i\omega t} \tag{2.29}$$

where x_0 is given by

$$x_0 = \frac{e}{m}\frac{E_0}{\omega_0^2 - \omega^2 - i\omega\gamma} \ . \tag{2.30}$$

The electric dipole moment for this harmonic oscillator is defined by

$$p(t) = ex(t) \tag{2.31}$$

If the medium is considered as a collection of N identical harmonic oscillators per unit volume, then the electric polarization of this medium becomes

$$P(t) = eNx(t) \tag{2.32}$$

So, the electric polarization is

$$P(t) = \frac{Ne^2}{m} \frac{E_0 e^{-i\omega t}}{\omega_0^2 - \omega^2 - i\omega t} \tag{2.33}$$

This equation can be rewritten in a more compact form in terms of the linear electric susceptibility, $\chi_e(\omega)$, of the medium

$$P(t) \equiv \varepsilon_0 \chi_e(\omega) E_0 e^{-i\omega t} \tag{2.34}$$

where ε_0 is the permittivity of free space.

The overall polarization is proportional to the applied electric field

$$P(t) \propto E(t) \ . \tag{2.35}$$

So, the medium oscillates with the same frequency of the applied field. However, for strong fields, the oscillation amplitudes become larger and this results in nonlinear motion of electrons. This is the case in the terahertz generation by optical rectification.

Equation of motion under influence of intense fields can be approximated by adding a small nonlinear term αx^2 to the Lorentz model described above [48]. If this nonlinear term is included as a perturbation to the potential, the nonlinear equation of motion becomes

$$\frac{d^2x}{dt^2} + \gamma \frac{dx}{dt} + \omega_0^2 x + \alpha x^2 = -\frac{e}{m} E(t) \tag{2.36}$$

under the influence of a monochromatic incident wave

$$E(t) = E_0 e^{-i\omega t} \tag{2.37}$$

where E_0 is the field amplitude. Since we have assumed that the nonlinear term is αx^2 very small compared to the linear one $\omega_0^2 x$, $x(t)$ can be expanded as a power series

$$x(t) = \sum_{n=1}^{\infty} x^{(n)}(t) \ , \qquad n = 1,2,3,... \ . \tag{2.38}$$

Assuming a convergent solution, with $x^n \propto {E_0}^n$, and $x^{(1)} \rangle\rangle x^{(2)} \rangle\rangle x^{(3)} \rangle\rangle ...$, the resulting equations for the first and second order terms becomes

$$\frac{d^2 x^{(1)}}{dt^2} + \gamma \frac{dx^{(1)}}{dt} + \omega_0^2 x^{(1)} = -\frac{e}{m} E(t) \ , \tag{2.39}$$

$$\frac{d^2 x^{(2)}}{dt^2} + \gamma \frac{dx^{(2)}}{dt} + \omega_0^2 x^{(2)} = -\alpha \left[x^{(1)} \right]^2 \ . \tag{2.40}$$

The linear response at ω corresponds to the first order term [48], so

$$x^{(1)}(t) = -\frac{e}{m} \frac{E_0 e^{-i\omega t}}{\omega_0^2 - \omega^2 - i\omega\gamma} + C \tag{2.41}$$

where C denotes the constant coefficients. The nonlinear response of the medium can now be calculated by inserting Equation (2.41) into Equation (2.40):

$$\begin{aligned} x^{(2)}(t) = &-\left(\frac{eE_0}{m} \right)^2 \frac{e^{-2i\omega t}}{({\omega_0}^2 - \omega^2 - i\gamma\omega)^2 (\omega^2 - 4\omega^2 - 2i\gamma\omega)} + C \\ &-\left(\frac{e}{m\omega_0} \right)^2 \frac{|E_o|^2}{({\omega_0}^2 - \omega^2)^2 + \gamma^2 \omega^2} \end{aligned} \ . \tag{2.42}$$

This Equation (2.42) can be interpreted as a sum of two terms $x_s^{(2)}$ and $x_d^{(2)}$:

$$x^{(2)}(t) = x_s^{(2)} + x_d^{(2)} \ . \tag{2.43}$$

where the subscript *s* denotes sum frequency and subscript *d* denotes to difference frequency.

The nonlinear response corresponding to optical rectification is the term $x_d^{(2)}$, which is given by

$$x_d^{(2)} = -2\alpha\left(\frac{e}{m\omega_0}\right)^2 \frac{|E_o|^2}{(\omega_0^2 - \omega^2)^2 + \gamma^2\omega^2} \tag{2.44}$$

The overall polarization due to optical rectification, $P_{O.R.}^{(2)}$ is

$$\begin{aligned} P_{O.R.}^{(2)} &= -eNx_d^{(2)} \\ P_{O.R.}^{(2)} &= \frac{2\alpha e^2 |E_0|^2 N}{m^2\omega_0^2\left[(\omega_0^2 - \omega^2)^2 + \gamma^2\omega^2\right]} \\ P_{O.R.}^{(2)} &= 2\varepsilon_0\chi^{(2)}|E_0|^2 \end{aligned} \tag{2.45}$$

where the term $\chi^{(2)}$ is the second-order susceptibility of the optical rectification [48].

In summary, the electric polarization, **P** in a material is proportional to the applied electric field **E**, and the electric susceptibility χ(E) through the relationship

$$\mathbf{P} = \varepsilon_0\chi(E)\mathbf{E} \tag{2.46}$$

The nonlinear effects, however, depend on the second or third order terms in the expansion of χ(E) in this equation

$$\mathbf{P} = \varepsilon_0(\chi^{(1)} + \chi^{(2)}E + \chi^{(3)}E^2 + \chi^{(4)}E^3 + ...)\mathbf{E} \qquad (2.47)$$

Optical rectification is a second order nonlinear effect and described by the $\chi^{(2)}E$ term in the expansion. It is also possible to generate THz radiation by the $\chi^{(3)}$ effect, but this method is not common [47].

Optical rectification techniques generally produce less power than photoconductive antennas. However, they emit in a broader bandwidth than photoconductive antennas.

2.3.2. THz Pulse Detection Methods

In THz Time-Domain Spectroscopy systems, two methods of THz pulse detection are widely used. These are the photoconductive detection antennas and the electro-optic sampling. In this thesis study, both of these methods were used.

2.3.2.1. Photoconductive Antennas

The purpose of radiation detector antennas is to transform electromagnetic waves into electrical signals. As in the case of THz emitting photoconductive antennas, THz detection with photoconductive antennas is also based on the rapid change in conductivity of a fast response material with the optical excitation by ultra-fast laser pulses. The ultra-fast laser source creates charge carriers inside the semiconductor, and the incoming THz pulse accelerates the charge carriers towards the electrodes of the antenna. The change of potential is measured with the aid of a lock-in amplifier.

2.3.2.2. Electro-Optic Sampling

Electro-optic sampling (EOS) is based on the linear electro-optic effect which is also called Pockel's effect. This effect describes the change of polarization due to an induced birefringence in the material [14 – 19].

The electric field of the THz field changes the refractive index along one of axes of the detection crystal. This change is proportional to the strength of the THz field along that axis and related to the first order susceptibility of the crystal. Therefore, the THz field induces birefringence which alters the polarization of the probe beam which is propagating collinearly with the THz beam inside the crystal. After the crystal, a quarter-wave-plate (QWP), a Wollaston prism (WP), and a balanced photodetector is used to determine the change in the polarization as illustrated in Figure 2.12.

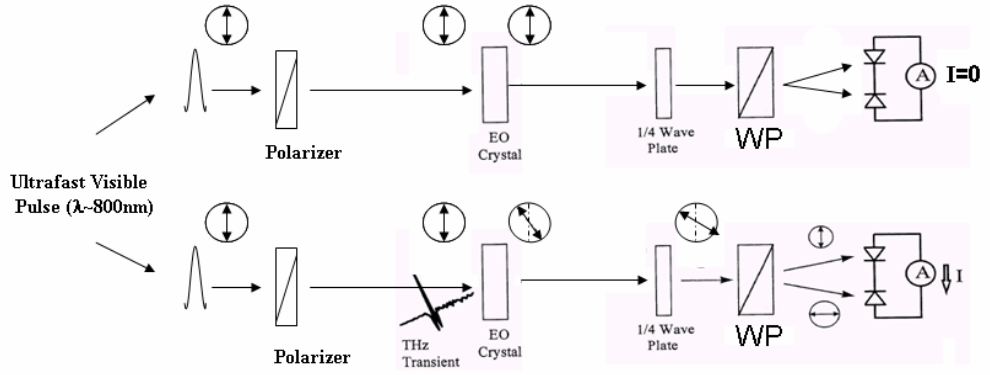

Fig.2.12. Electro-Optic Sampling

The electro-optical properties and the thickness of the crystal directly affects the frequency response and the sensitivity. The thickness should provide enough interaction length and good group-velocity mismatch, in order to achieve higher detection bandwidth [49].

2.4. Typical THz-TDS configurations

In this thesis, several different THz-TDS configurations are used to get the optimum performance for the spectroscopic measurements. The properties of these THz spectrometers were investigated under a three year project "*Development of a Compact Time-Domain Terahertz Spectrometer*" {TÜBİTAK - TBAG (Basic Sciences Reseach and Development) 1001 project No. 107T742} which is supported by the Scientific and Research Council of Turkey (TÜBİTAK). The main aim of this project is the production and development of the first-ever terahertz generation and detection systems in Turkey. Each of the constructed terahertz time-domain spectrometer configurations described below has its own advantages and disadvantages.

2.4.1. THz Spectroscopy system based on photoconductive antenna generation and photoconductive antenna detection

In THz-TDS system, a Lt-GaAs based photoconductive antenna with a dipole gap of 6 μm is used to generate the THz radiation as explained in section 2.3.1.1. The radiation is detected by another photoconductive antenna of the same type as explained in section 2.3.2.1. This spectrometer can be driven by either a Ti: Sapphire laser or an Erbium-doped fiber laser, since it does not require too much power to drive the antenna. An ultra-fast laser capable of producing powers around 40 - 50 mW is enough to be used in this system, since the damage threshold of the antennas is about 40 mW, so 30 - 35 mW for generation arm and 5 - 10 mW for the detection arm is suitable for the system to work efficiently. The generation and detection beams are focused into the dipole gaps of the antennas by using 20x objectives. The emitter is AC modulated with the aid of a function generator in order to facilitate lock-in detection. The photoconductive antennas used in this configuration are shown in Figure 2.13 and the experimental setup used for this system is shown in the Figure 2.14.

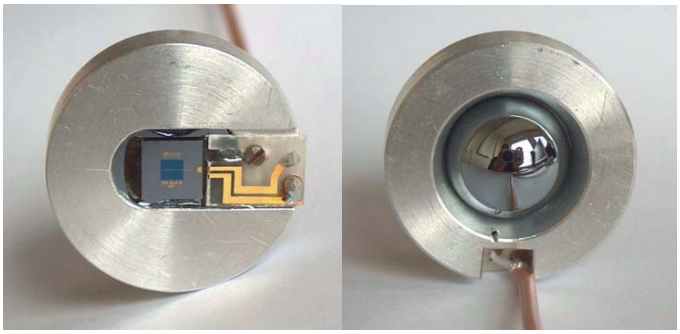

(*Photo reference: http://www.batop.de/)*

Fig.2.13. Terahertz Photoconductive Antenna

This system is capable of producing a bandwidth up to 1.7 THz. If used with the Er-doped fiber lasers, this configuration provides a low-cost, turn-key, and compact solution for THz-TDS studies. In Figure 2.15, the time-domain profile for air is shown. This profile of 140 ps corresponds to 21 mm scanning length of the delay stage. The Fourier transformed spectrum is shown in Figure 2.16.

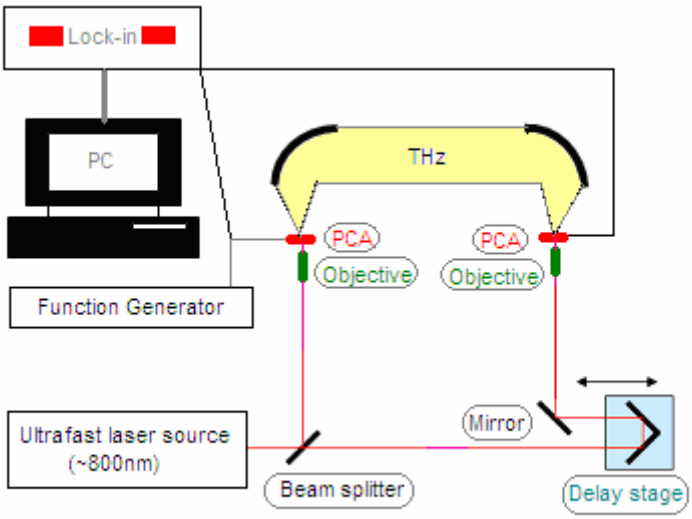

Fig.2.14. THz-TDS system based on PCAs.

The time-domain profile for the main peak is broader compared to the one using electro-optic sampling for detection (see Figure 2.15), this is because of the limitations in the signal response due to the time constants of carrier

dynamics of the photoconductor antenna [47]. The frequency range is up to 2.3 THz which can be seen from the Figure 2.16.

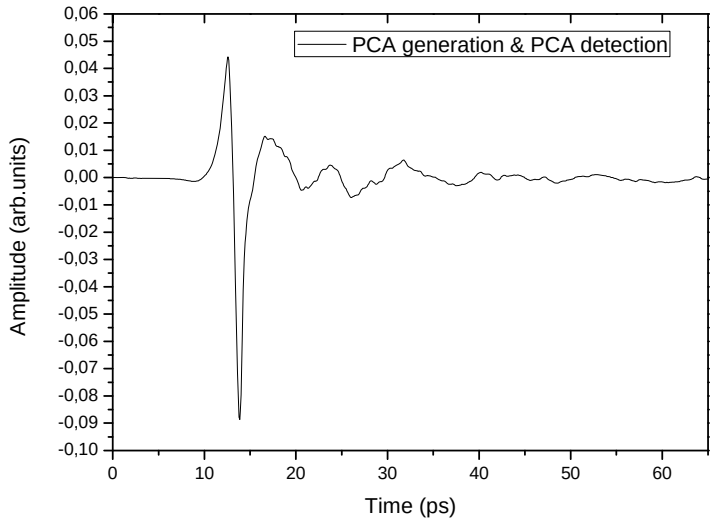

Fig.2.15. The time-domain profile for air of the THz-TDS using photoconductive antenna generation and electro-optic sampling detection

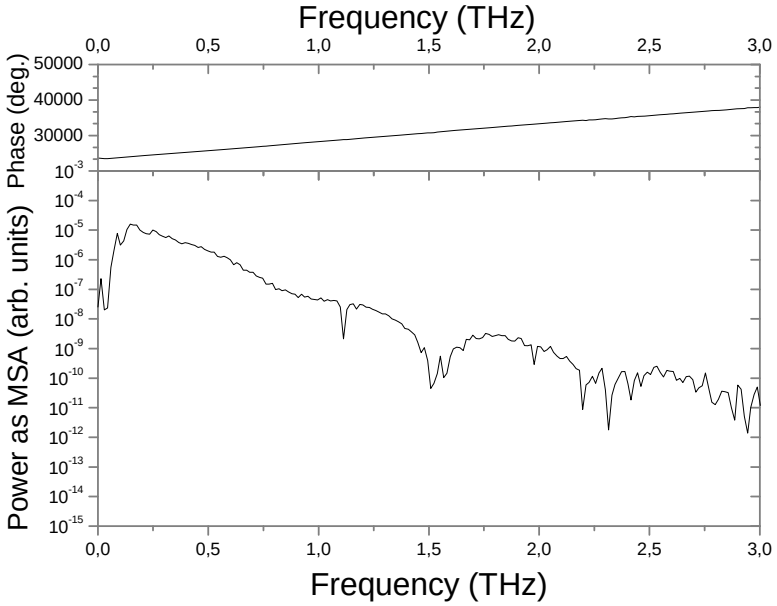

Fig.2.16. The frequency spectrum for air of the THz-TDS using PCA generation and PCA detection (MSA: Mean Square Amplitude)

2.4.2 THz Spectroscopy system based on photoconductive antenna generation and electro-optical detection

In a THz-TDS system, a Lt-GaAs based photoconductive antenna with a dipole gap of 6 μm is used to generate the THz radiation as explained in section 2.3.1.1. The emitting antenna is AC modulated by using a function generator. The radiation is detected by electro-optic sampling method as explained in section 2.2.2. For this reason, an isotropic ZnTe <110> crystal is used for the terahertz beam to induce birefringence along the principal axes of the crystal. The thickness of the ZnTe is chosen according to best phase matching conditions. The elliptically polarized beam after passing a quarter wave plate is separated into two components by a Wollaston prism and detected by a balanced photodetector with the aid of a lock-in amplifier.

The experimental setup used for this system is illustrated in the Figure 2.17 and the time-domain profile for air is shown in Figure 2.18. The frequency spectrum is presented in Figure 2.19.

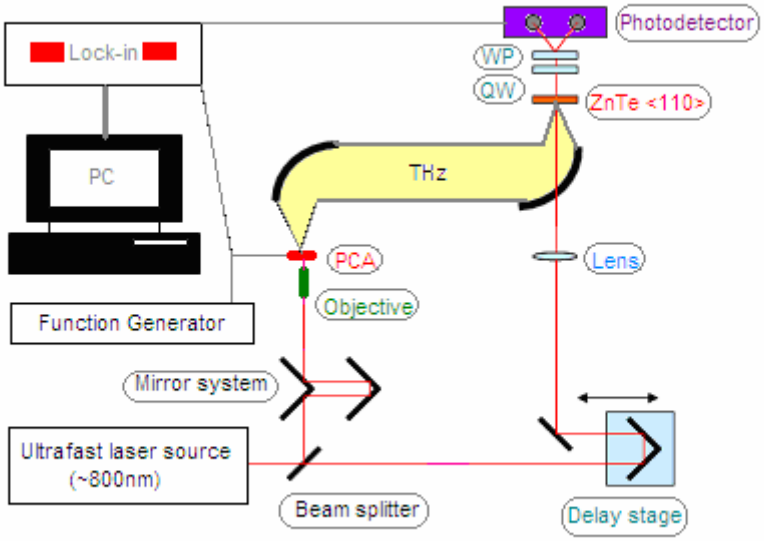

Fig.2.17. THz-TDS based on antenna generation and electro-optic sampling

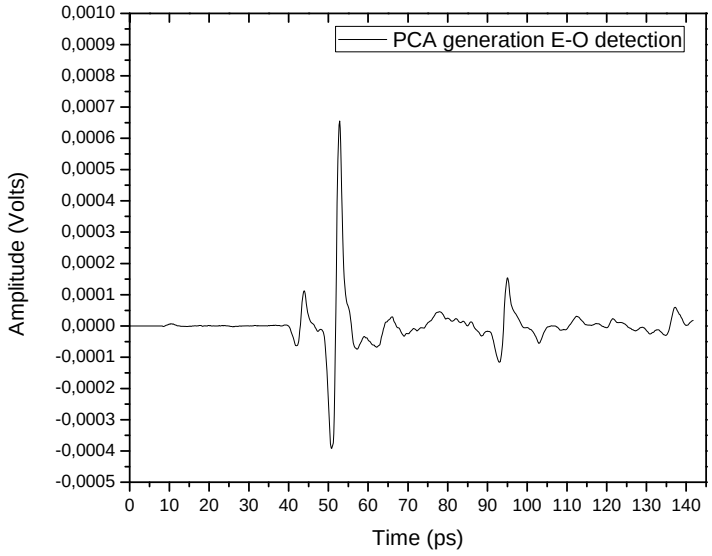

Fig.2.18. The time-domain profile for air with the THz-TDS using photoconductive antenna for generation and electro-optic sampling for detection.

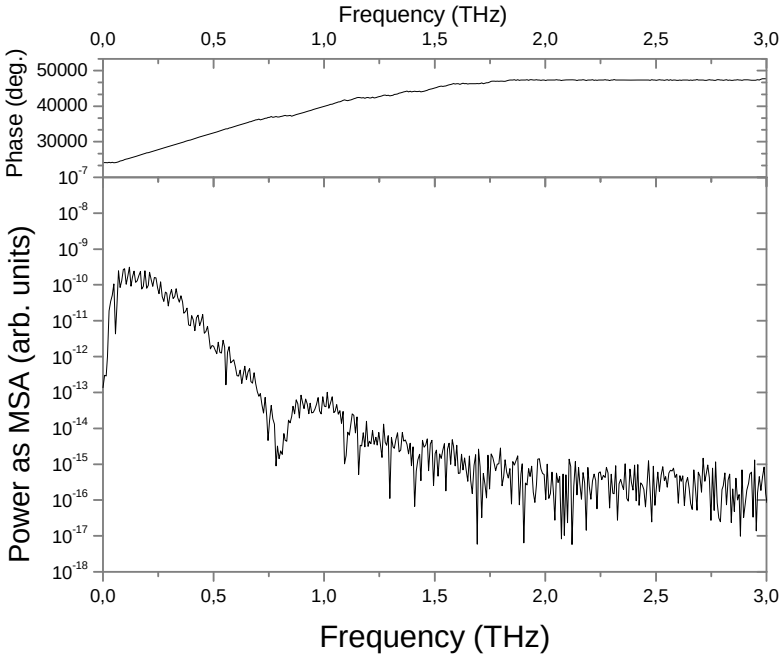

Fig.2.19. The frequency spectrum for air of the THz-TDS using photoconductive antenna for generation and electro-optic sampling for detection. (MSA: Mean Square Amplitude)

This system is also capable of producing a bandwidth of 2 THz as shown in Figure 2.19, but more sensitive for detection with respect to the previous system using hotoconductive antenna as a detector. Both the Ti: Sapphire and Er-doped lasers can be used in this configuration, since they have capable of providing enough laser power for photoconductive antenna generation. Actually, the Ti:Sapphire lasers produces more than enough power, so the laser power should be reduced below the damage threshold of the photoconductive antenna in order to prevent any damage to the antenna. This is generally done by using filters or beam splitters. For the photoconductive antennas used in this thesis, the damage threshold is about 40 mW while the Ti:Sapphire laser produces powers around 360 mW.

2.4.3. THz Spectroscopy system based on optical rectification and electro-optic sampling via difference frequency mixing

In a THz-TDS system, the optical rectification is applied in order to produce broadband THz radiation. The detection of this broadband emission is generally done by electro-optic sampling.

The optical rectification is achieved by focusing a powerful near infrared femtosecond laser pulse which is modulated by an optical chopper on to the ZnTe <110> crystal by using a proper lens as explained in Section 2.3.1.2. The system is illustrated in Figure 2.20.

Since more power is needed to achieve optical rectification, Ti: Sapphire lasers are generally used in this type of THz-TDS. This configuration allows bandwidths up to 5.3 THz where the ZnTe has an optical phonon resonance [50]. However, the emitted THz powers are quite low with compared to the previous THz-TDS configurations.

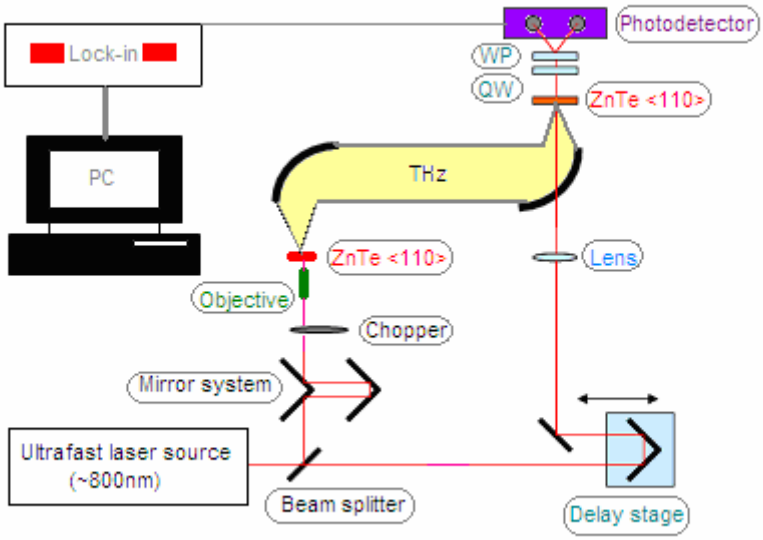

Fig.2.20. THz-TDS based on optical rectification and electro-optic sampling

The physical characteristics of the generation crystal used in optical rectification have very important effects on the properties of the emitted radiation. Especially, the efficiency depends on the phase-matching conditions. We have performed THz-generation based on this technique with different crystal thicknesses. The data for generation with 1 mm and 2 mm thick crystals are shown in Figures 2.21 - 24. These scan were taken for 70 ps which correscponds to a scanning length of 10.5 mm. The main THz peaks are around 1 THz. If compared with the photoconductive antenna generation (see Figures 2.15 - 19), the THz signal is weaker in optical rectification. However, the electro-optic generation offers ultra-broadband emission. The response of the medium to the pump beam is nearly instantaneous [50].

The alignment of the system is easier than photoconductive antennas, but it is important to avoid the Fabry-Perot oscillations originating from both of the generation and detection crystals. In chapter 5, we shall present a method on how to remove these “etalon” effects by applying an algorithm.

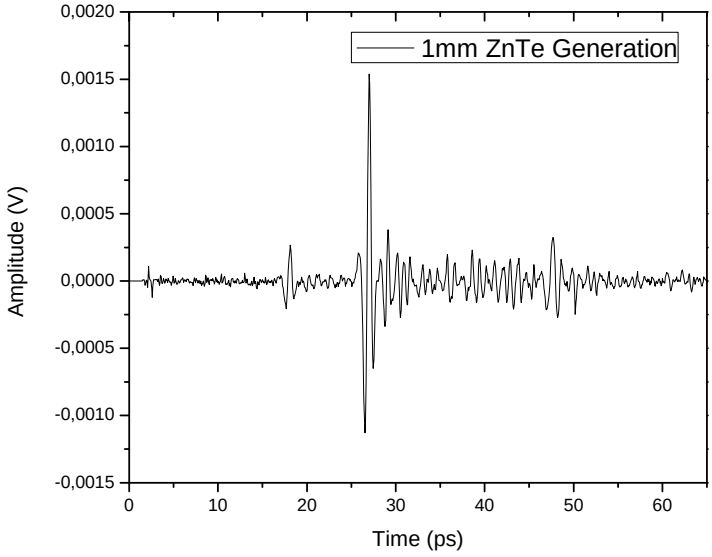

Fig.2.21. THz time domain pulse profile produced by 1 mm ZnTe <110> in air

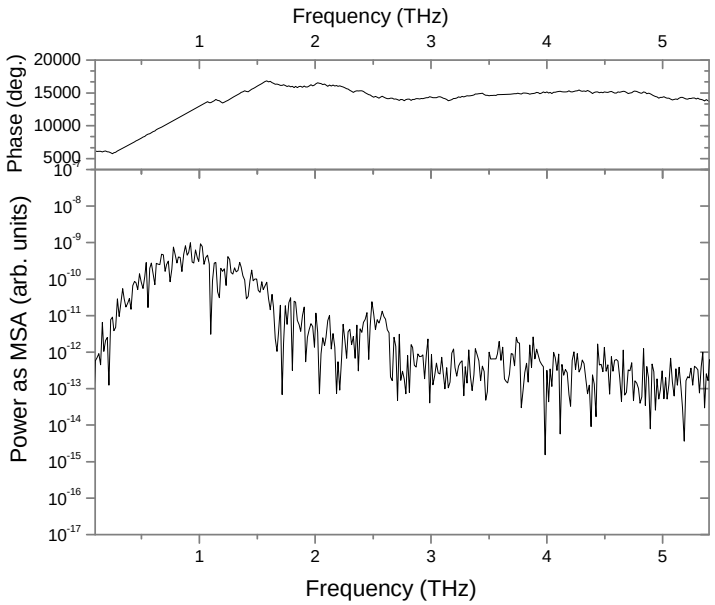

Fig.2.22. THz-pulse FFT profile produced by 1 mm ZnTe <110> in air
(MSA: Mean Square Amplitude)

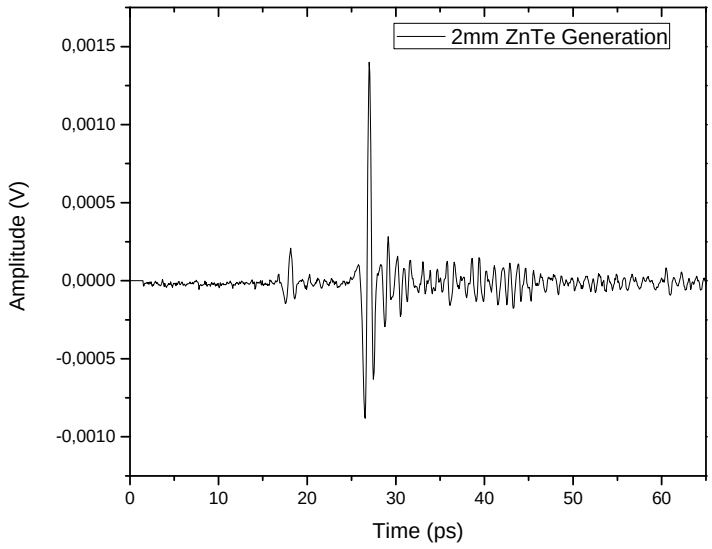

Fig.2.23. THz time domain pulse profile produced by 2 mm ZnTe <110> in air

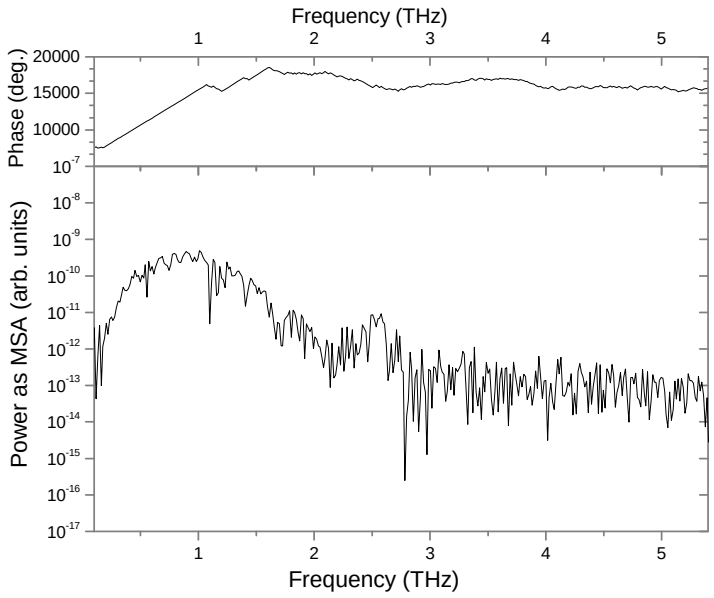

Fig.2.24. THz-pulse FFT profile produced by 2 mm ZnTe <110> in air
(MSA: Mean Square Amplitude)

2.5. Terahertz Time-Domain Spectral Analysis

The characteristics of the medium under investigation are obtained coherently from the terahertz time-domain data. The time-dependent THz electric field is given by

$$E(z,t) = \frac{1}{\sqrt{2\pi}} \int_{-\infty}^{+\infty} E(z,\omega) \cdot e^{-i\omega t} \, d\omega \ , \tag{2.48}$$

in the time-domain. On the other hand, in the frequency domain, the electric field is given by

$$E(z,\omega) = \frac{1}{\sqrt{2\pi}} \int_{-\infty}^{+\infty} E(z,t) \cdot e^{-i\omega t} \, dt \ . \tag{2.49}$$

So, the electric field can be written as

$$E(z,t) = A(z,\omega) \cdot e^{i\varphi(\omega)} \tag{2.50}$$

where $A(z,\omega)$ is the amplitude. From this equation, it can be stated that the terahertz time-domain spectrum not only provides the amplitude information but also the phase [51].

The THz-TDS measures the difference in the amplitude and phase of the terahertz field to determine the imaginary and real refractive indices, permittivity or conductivity of the medium under investigation. To do this, the THz spectrum of the dispersive medium is compared with the free space (reference) THz spectrum. Generally, the THz-TDS systems produces powers of microwatts, the corresponding electric fields are on the order of 1 $V \cdot cm^{-1}$. For this reason, the interaction of the dispersive medium with the THz field can

be assumed linear, so the Maxwell's equations can be used to extract the material parameters from the experimentally measured THz pulse electric fields $E(z,t)$ with and without the sample.

The profile of the THz radiation is detected by varying the time delay. The profile of the reference $E_{REF}(t)$ and the sample $E_{sample}(t)$ Fourier transformed to the frequency domain as $\tilde{E}_{REF}(\omega)$ and $\tilde{E}_{sample}(\omega)$ [52, 53]. The ratio of $\tilde{E}_{REF}(\omega)$ and $\tilde{E}_{sample}(\omega)$ is written in terms of the power transmittance $T(\omega)$, the phase change $\Delta\phi$ and the thickness of the sample l as

$$\frac{\tilde{E}_{sample}(\omega)}{\tilde{E}_{REF.}(\omega)} = \left|\sqrt{T(\omega)}\right| \exp\left\{-i\left[\Delta\phi(\omega) - \frac{\omega l}{c}\right]\right\} \tag{2.51}$$

This equation can be written as [52]

$$\frac{\tilde{E}_{sample}(\omega)}{\tilde{E}_{REF.}(\omega)} = 4\frac{\tilde{n}(\omega)}{\left[\tilde{n}(\omega)+1\right]^2} \frac{\exp\left\{-\frac{i\omega l}{c}\left[\tilde{n}(\omega)-1\right]\right\}}{\left\{1-\left(\frac{\left|\tilde{n}(\omega)-1\right|}{\left|\tilde{n}(\omega)+1\right|}\right)^2 \exp\left[-i\frac{2l\omega}{c}\tilde{n}(\omega)\right]\right\}} \tag{2.52}$$

where $\tilde{n}(\omega) = n(\omega) - ik(\omega)$ is the complex refractive index and c is the speed of light in vacuum.

Since the power transmittance $T(\omega)$ and the phase shift $\Delta\phi$ are measured in the terahertz transmission experiments, the refractive index of the sample $n(\omega)$ and $k(\omega)$ can be calculated. From the complex refractive index, the complex

dielectric constant of the sample $\tilde{\varepsilon}(\omega) = \varepsilon_1(\omega) - i\varepsilon_2(\omega)$ can be determined from the equation

$$\tilde{\varepsilon}(\omega) = \left[\tilde{n}(\omega)\right]^2 . \tag{2.53}$$

Furthermore, the complex conductivity of the sample is written as

$$\tilde{\sigma}(\omega) = \sigma_1(\omega) - i\sigma_2(\omega) \tag{2.54}$$

where $\sigma_1(\omega) = \varepsilon_0 \omega \varepsilon_2(\omega)$ and $\sigma_2(\omega) = -\varepsilon_0 \omega[\varepsilon_1(\omega) - \varepsilon_\infty]$ with ε_0 is the permittivity of the free space and ε_∞ is the dielectric constant of the sample at very high frequencies [54].

By applying the terahertz analysis, the optical properties of materials such as dielectric constant and conductivity can be extracted from the terahertz transmittance and phase change of the material. Compared to the Fourier Transform Spectroscopy, the THz-TDS measures phase as well as amplitude. THz-TDS has the advantage of avoiding the uncertainties of the Kramers-Kronig analysis, we also have a high signal-to-noise ratio of THz-TDS measurements [55].

The terahertz time-domain analysis outlined here was applied for the characterization of nominally undoped GaAs samples grown by molecular beam epitaxy and ZnTe crystals. The measurements and calculations of these studies will be presented in the chapter four and five.

CHAPTER 3

ELECTRICAL CHARACTERIZATION OF MBE GROWN EPITAXIAL GaAs

3.1. Introduction

This chapter summarizes the measurements for the electrical characterization of the nominally undoped epitaxial GaAs samples grown by molecular beam epitaxy. These measurements are based on the van der Pauw technique and the Hall effect measurements. These measurements are made according to the "*ASTM* (American Society for Testing and Materials) *standards*" [56]. All these measurements were done by using ohmic contacts. The material parameters measured and calculated using these techniques compared to that of the THz time-domain spectroscopic measurements which does not require electrical contacts. The comparison of the classical techniques and THz spectroscopic measurements will be discussed in the next chapter.

3.2. The van der Pauw Technique

In 1958, L.J. van der Pauw developed a technique which is quite practical and reliable to measure the galvanometric parameters of uniform samples. In its original form, the technique is for the measurement of resistivity and Hall

coefficients on lamellae of arbitrary shape [57], and for measuring specific resistivity and Hall effect of disks of arbirtrary shape [58]. Generally, van der Pauw's technique is applied together with Hall effect measurements.

In order that the van der Pauw technique to be applied, the samples should be uniform and thin, the contacts have to be very small, ohmic, and located at the circumference of the samples. The shape of the samples may be arbitrary but homogeneous and singly connected, so that there are no nonconducting or isolated holes in the sample. In practice, the contacts are preferably done symmetrically [57] as shown in Figure 3.1 [56].

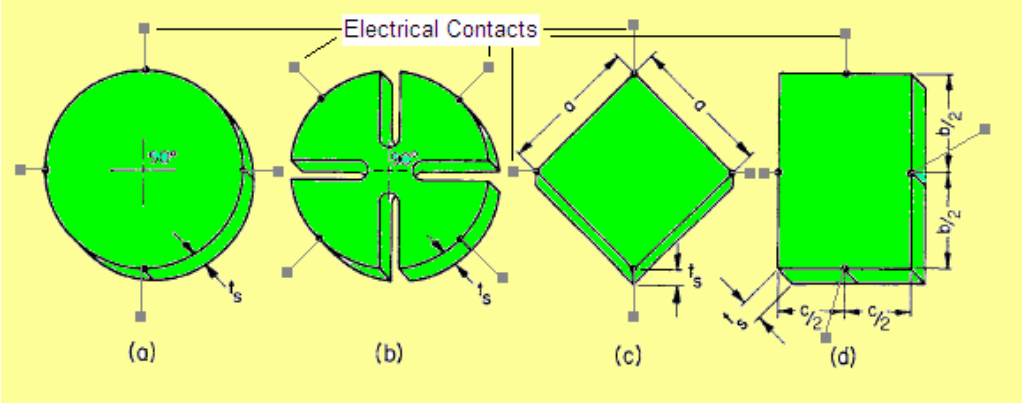

Fig.3.1. Typical symmetrical sample geometries (a. disk, b. cloverleaf, c. square or rectangle with contacts at the corners, d. square or rectangle with contacts at the edges) for van der Pauw and Hall effect measurements

In the van der Pauw measurements, the aim is to determine the sheet resistance (R_s) of the sample. This is done by measuring the corner-to-corner resistances (R_A and R_B) from the Ohmic contact points as shown in Figure 3.2.

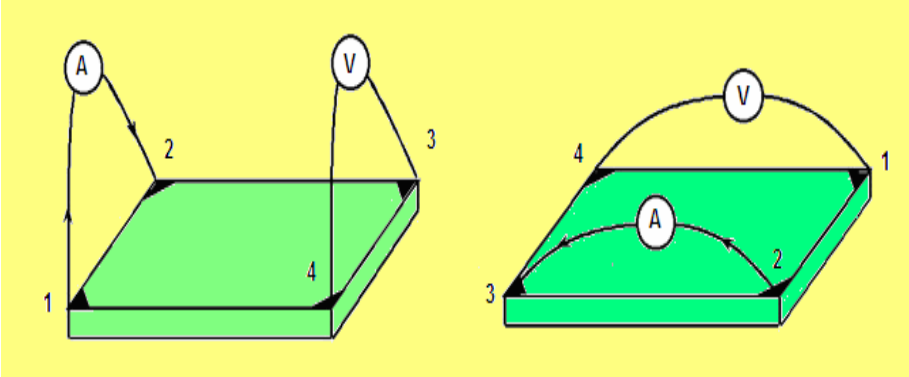

Fig.3.2. Determination of R_A and R_B

To measure R_A and R_B, a dc-current, I_{12}, is applied between the contacts 1 and 2 (from 1 to 2), while the corresponding voltage V_{34} is measured. Then, a dc-current I_{23} (from 2 to 3) is applied between the contacts 2 and 3, while the corresponding voltage V_{14} is measured. From these measurements, the R_A and R_B are calculated:

$$R_A = \frac{V_{43}}{I_{12}} \text{ and } R_B = \frac{V_{14}}{I_{23}} \ . \tag{3.1}$$

The sheet resistance (R_s) is, then, calculated by the equation

$$\exp(-\pi \frac{R_A}{R_S}) + \exp(-\pi \frac{R_B}{R_S}) = 1 \ . \tag{3.2}$$

This equation is solved numerically by iteration techniques. From the sheet resistance and the thickness of the sample (l), the resistivity is calculated by

$$\rho = R_S l \ . \tag{3.3}$$

The accuracy of the measurements is generally improved by applying current in all combinations (I_{12}, I_{23}, I_{34}, I_{41}, I_{21}, I_{32}, I_{43}, I_{14}) and measuring the

corresponding voltages (V_{34}, V_{41}, V_{12}, V_{23}, V_{43}, V_{14}, V_{21}, V_{32}). Then, the eight resistance values ($R_{12,34}=V_{34}/I_{12}$, $R_{23,41}=V_{41}/I_{23}$, $R_{34,12}=V_{12}/I_{34}$, $R_{41,23}=V_{23}/I_{41}$, $R_{21,43}=V_{43}/I_{21}$, $R_{32,14}=V_{14}/I_{32}$, $R_{43,21}=V_{21}/I_{43}$, $R_{14,32}=V_{32}/I_{14}$) are calculated. The resistance values corresponding to the change in the polarization of the current are to be equal; $R_{12,34}=R_{21,43}$, $R_{23,41}=R_{32,14}$, $R_{34,12}=R_{43,21}$, $R_{41,23}=R_{14,32}$. In addition, $R_{12,34} + R_{21,43} = R_{34,12} + R_{43,21}$ *and* $R_{23,41} + R_{32,14} = R_{41,23} + R_{14,32}$ due to the reciprocity theorem [59]. So, these calculations should give consistent values if the measurements are done properly. Otherwise, the error sources should be investigated. In this sense, the van der Pauw technique also serves as a consistency check.

The sheet resistance, then, is calculated from R_α and R_β which are determined from the eight resistance measurements as follows:

$$R_\alpha = \frac{1}{4}\left(R_{12,34} + R_{21,43} + R_{34,12} + R_{43,21}\right)$$

and (3.4)

$$R_\beta = \frac{1}{4}\left(R_{23,41} + R_{32,14} + R_{41,23} + R_{14,32}\right)$$

So, the van der Pauw equation to be solved becomes

$$\exp(-\pi \frac{R_\alpha}{R_S}) + \exp(-\pi \frac{R_\beta}{R_S}) = 1 \qquad (3.5)$$

From the numerical solution of this equation and the known sample thickness (l), the resistivity is determined from the equation

$$\rho = R_S l \qquad (3.6)$$

3.3. The Hall Effect

In 1879, E.H. Hall discovered an interesting physical phenomenon [60] which led to lots of applications such as Hall pick-ups, Hall magnetometers, heavy-current ampermeters, and signal transducers. The discovery of the Hall effect has turned out to be a practical method for measuring the electrical properties of semiconductor materials. The concentration, mobility and the sign of the majority charge carriers can be determined by Hall effect measurements [56].

If a particle with charge q moves at velocity **v** under a magnetic field **B**, the force acting on this particle due the magnetic field is given by

$$\mathbf{F}_{\text{mag.}} = \mathrm{q}\mathbf{v} \times \mathbf{B} \tag{3.7}$$

If there is also an electric field acting on that particle, the total force acting on it becomes,

$$\mathbf{F} = q(\mathbf{E} + \mathbf{v} \times \mathbf{B}) \tag{3.8}$$

This force is called the Lorentz force. It is the Lorentz force that lies behind the Hall effect.

For an n-type sample of rectangular cross section, the majority charge carriers are electrons. If a constant current density **J** is applied to the sample in the $+x$ direction under the magnetic field **B** in the $+z$ direction, the electrons will drift towards the $-y$ direction, which in turn causes a negative charge accumulation on this side. So, this causes a potential difference across the sides of the sample. This potential difference is called the Hall voltage, V_H. For a p-type sample, positive charge accumulation occurs on the same side, since

their velocity is in –*x* direction. So, the Hall voltage is negative for n-type samples, and positive for p-type samples as shown in Figure 3.3 [56].

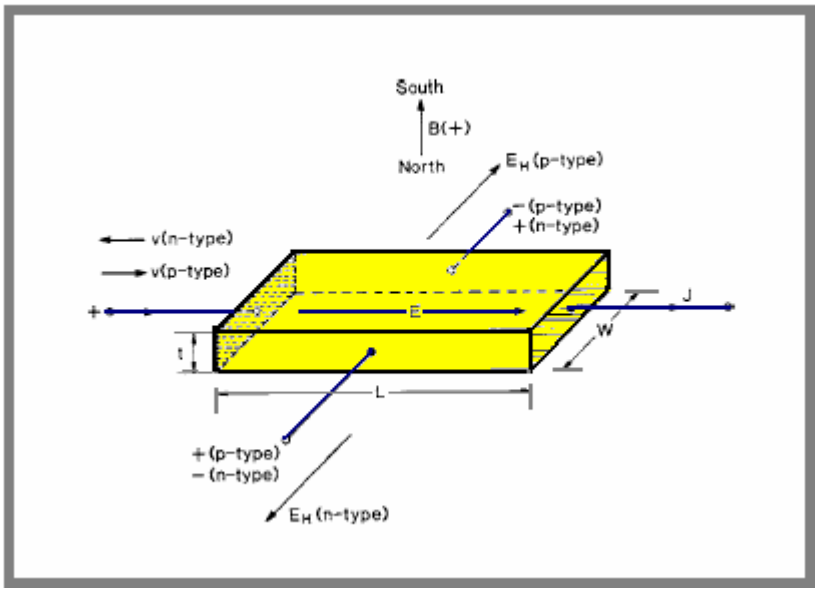

Fig.3.3. The Hall effect

The magnitude of the Hall voltage is given by

$$V_H = \frac{IB}{qnl} \quad or \quad V_H = \frac{IB}{qn_S} \tag{3.9}$$

where l is the sample thickness, n is the charge density and $n_S = nl$ is the sheet charge density. So, the measurement of the Hall voltage, V_H, from the known values of *q*, *I*, and *B*, leads to determination of the sheet charge density. Using the previously described van der Pauw technique, the sheet resistance of the sample R_S can be determined. Knowing the sample thickness (l) leads to determination of the resistivity, ρ and the charge density, n which is given by $n = \frac{n_S}{l}$.

The Hall mobility is then calculated by

$$\mu = \frac{V_H}{IBR_S} = \frac{1}{qn_S R_S} \tag{3.10}$$

This equation can also be expressed in terms of the conductivity σ and the Hall coefficient R_H, which is defined by

$$R_H = \frac{V_H l}{IB} \ . \tag{3.11}$$

So, the mobility is written as

$$\mu = R_H \sigma \ . \tag{3.12}$$

3.4. Experiment

If the value of the applied magnetic field, the current, and the dimensions of the sample is known, the Hall coefficient can be determined by measuring the Hall voltage induced in the sample. From the numerical value and the sign of the Hall coefficient R_H, the concentration and the sign of the majority charge carriers can be calculated. For p-type semiconductors, the Hall coefficient is positive, and for n-type semiconductors, the Hall coefficient is negative. In addition to these, if the conductivity σ of the sample is measured under the magnetic field, the Hall mobility μ of the majority charge carriers can also be calculated from the formula:

$$\mu = R_H \sigma \ . \tag{3.13}$$

For this reason, the Hall effect measurements together with the van der Pauw technique is the major method in determining the electrical characteristics of semiconductor materials.

In this thesis, the measurements were done by the setup shown in Figure 3.4. The magnetic field is created by using an H-yoke electromagnet which is driven by a magnet power supply capable of supplying currents up to 100 A. The magnet power supply and the coils of the electromagnet are water cooled. The electromagnet is calibrated so that a current of 60 A creates a magnetic field of 0.9 T. The samples were placed perpendicular to the magnetic field, at the center of the magnetic poles of the magnet.

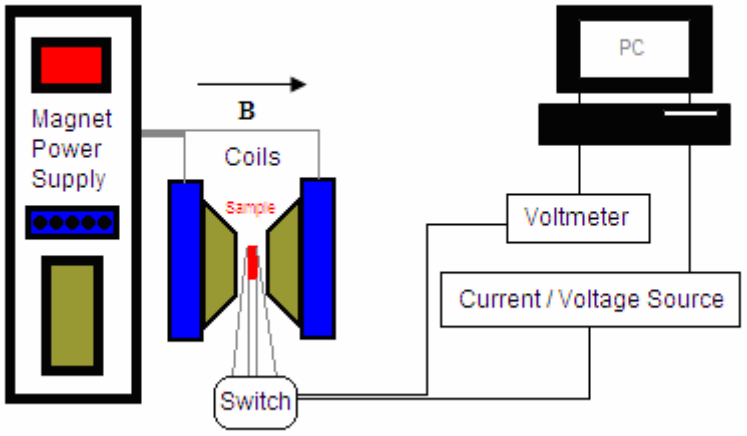

Fig.3.4. Setup for Hall effect and van der Pauw measurements

The epitaxial nominally undoped GaAs samples were grown at 600 ^{o}C to a 1 μm effective layer thickness on top of a 650 μm thick SI-GaAs wafer. To obtain accurate data, very small (less than 1 mm^2) AuGe Ohmic contacts were devised at the corners of the square shaped (1.4 cm x 1.4 cm) GaAs sample. All the contacts were checked to be of similiar resistance. From these contact

points, the sample was connected to a switch box with the similar nonmagnetic wiring materials to easily change the current application and voltage detection points as shown in Figure 3.5. The swithed box is connected to a programmable current/voltage source (Keithley Model 220) and an electrometer/multimeter (Keithley Model 619). These devices are controlled by a personal computer with data acquisition software.

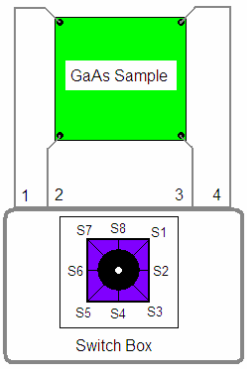

Switch Position	Current	Voltage
S1	I_{12}	V_{34}
S2	I_{23}	V_{41}
S3	I_{34}	V_{12}
S4	I_{41}	V_{23}
S5	I_{21}	V_{43}
S6	I_{32}	V_{14}
S7	I_{43}	V_{21}
S8	I_{14}	V_{32}

Fig.3.5. The switch box used to change the contact points

The samples were kept under uniform temperature conditions during the experiments, so that there were no temperature gradients between the contacts. The measurements were done at room temperature (300 K).

3.5. Results

The measurements were done under the magnetic field of $B = 0.97$ T = 9700 G. The current applied for the van der Pauw measurements was kept fixed at 420 nA, so only the polarity of the current was changed during the experiments. The current applied for the Hall effect measurements was also kept fixed at 870 nA, and only the polarity of the current was changed. These

measurements were repeated for the magnetic field of the same strength but its polarity was reversed. The data was taken as described above. The results for sample of 1 μm thickness are given in Table 3.1.

Table 3.1. The results for 1 μm thick nominaly undoped epitaxial GaAs

Resistivity	10.4 Ω.cm
Conductivity	0.096 $\Omega^{-1}.cm^{-1}$
Hall coefficient	5800 $cm^3.C^{-1}$
Charge carrier concentration	1.1 x 10^{15} cm^{-3}
Mobility	550 $cm^2.V^{-1}.s^{-1}$

The resistivity and conductivity values presented in this tables were measured and calcuted by the van der Pauw technique. From the Hall voltage measurements, the carrier concentration was found. So, the van der Pauw technique and Hall effect measurements led to determination of the mobility.

3.6. Discussion

GaAs is composed of gallium (Ga) and arsenic (As) atoms, and was synthesized in 1929 by Goldschmidt. Its structure is of zinc blende type. Figure 3.7 shows the unit cell of GaAs crystal lattice.

GaAs is one of the most widely used material in semiconductor industry, since GaAs is a direct gap semiconductor. Direct gap semiconductors can be used in light emitting diodes (LED), semiconductor lasers, and photodetectors.

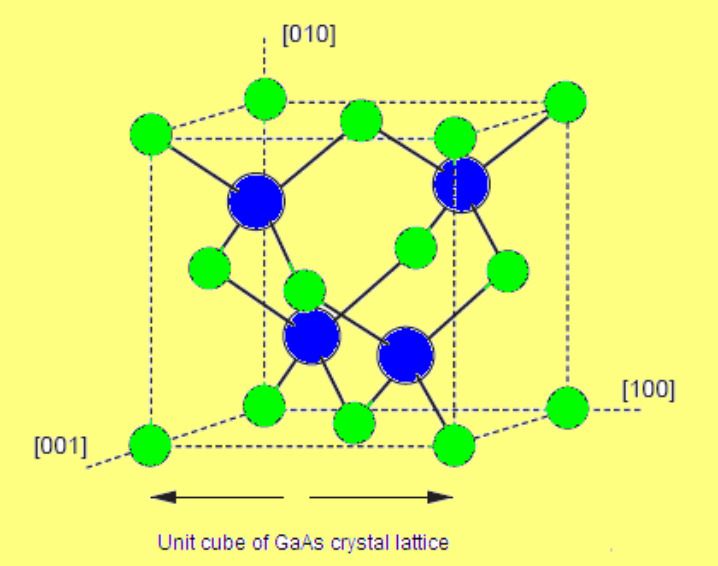

Fig.3.6. The GaAs structure

In Terahertz Science and Technology, it is one of the commonly used materials in the photoconductive antenna production. For this reason, the production and characterization of GaAs structure requires intense study for THz researchers. In this chapter, we have performed the electrical characterization of MBE grown GaAs samples. The consequences of these experiments will be in two folds. The first one, is to show the validity of THz spectroscopic measurements with respect to the electrical characterization methods. The second is to use these samples in photoconductive antenna production, especially, for THz detection. This second one is beyond the scope of this thesis, and left for future study.

The van der Pauw technique and the Hall effect measurements are efficient techniques to determine the conductivity type of the material (n or p), the density and mobility of the majority carriers if the thickness of the sample is well-determined. However, even though the technique is well-constructed, there exists several experimental limitations. The fluctuations in the sample temperature and the contact resistance problems are the commonly encountered

ones. Nonsymmetrical and nonuniform contacts introduce extra resistance to the measurement. The Ohmic contact production procedure also introduces some damage to the samples. The thickness of the samples is another difficulty, since their Hall voltage may be quite small. On the other hand, the samples should react to the applied currents quickly, so that during the changes in the applied current direction, the sample is to return its equilibrium state.

In conclusion, even though the van der Pauw and Hall effect measurements are well-established they are not perfect. In the next chapter, we shall investigate a noncontact method based on Terahertz time-domain spectroscopy.

CHAPTER 4

THz PROBE STUDIES OF MBE GROWN EPITAXIAL GaAs

4.1. Introduction

One of the major applications of THz-TDS is in material characterization. THz spectroscopy has been used to determine ultrafast carrier dynamics of doped semiconductors such as GaAs [61] and silicon wafers [62 - 65]. An important focus is on the measurement of the dielectric constant of thin films [66]. Epitaxially grown GaAs films using MBE methods have attracted much attraction due to their projected use in infrared imaging and detection systems.

The detection characteristics of THz pulses have been previously studied for photoconductive antennas and electro-optic detection. Among the photoconductive antennas, GaAs based ones are commonly used in THz generation and detection systems. Even though this type of semiconductor produces narrower bandwidth, it produces more power as compared with the electro-optic generation methods [67]. Both LT-GaAs and SI-GaAs based antennas produce powers of order submicrowatts under reasonable pump and bias conditions [68]. In order to increase the performance of GaAs based antennas, better production and characterization standards of these structure should be achieved.

In this study, we have demonstrated the efficiency of THz-TDS to measure the mobility and the carrier number density of MBE grown GaAs. In addition, from the photoexcitation measurements, we found that the photoexcitation increases the conductivity of the GaAs samples in addition to changes in the refractive index.

This chapter is organized as follows: In section 2, the Drude Model will be covered briefly. In section 3, we describe the experimental setups and procedure as well as the data collected by the Hall effect and THz spectroscopy measurements. In section 4, we present the analysis of data, and the critical parameters of the epitaxial grown GaAs. In the section 5, the results are discussed.

4.2. Drude Model

After the discovery of the electron by J.J. Thompson in 1897, Paul Drude developed a model for the electrons in metals before quantum theory in 1900. Even though, it is a quite simplistic model, it is still practical [69].

The Drude theory is constructed upon the adoptation of the kinetic theory of gases to the metals. The electrical and thermal conductivities of metals are explained by considering the electrons in metals as a gas of electrons [69]. The positive charges were assumed to be stationary and the interaction of electrons with the ions and the nucleus is considered to be that of hard sphere scattering. The probability of collision of an electron is assumed to be related to the relaxation time τ. So, an electron suffers a collison in any infinitesimal time interval, dt, with the probability of dt/τ. The electrons were assumed to reach thermal equilibrium via collisions.

If the wavelength of the electromagnetic field is large with respect to the mean free path of an electron, the Maxwell's equations can be written in the presence of a current density **J** as [69]

$$\nabla \cdot \mathbf{E} = 0 \ , \qquad \nabla \cdot \mathbf{B} = 0 \ ,$$
$$\nabla \times \mathbf{E} = -\frac{1}{c}\frac{\partial \mathbf{H}}{\partial \mathrm{t}} \ , \qquad \nabla \times \mathbf{H} = \frac{4\pi}{\mathrm{c}}\mathbf{J} + \frac{1}{\mathrm{c}}\frac{\partial \mathbf{E}}{\partial \mathrm{t}} \ . \tag{4.1}$$

If the field is assumed uniform throughout the mean free path, then **J** can be assumed as [69]

$$\mathbf{J}(\mathbf{r},\omega) = \sigma(\omega)\mathbf{E}(\mathbf{r},\omega) \tag{4.2}$$

where

$$\sigma(\omega) = \frac{\sigma_0}{1 - i\omega\tau} \tag{4.3}$$

is the frequency-dependent (AC) conductivity, and

$$\sigma_0 = \frac{ne^2\tau}{m} \tag{4.4}$$

is the frequency-indepenedent (DC) conductivity. Then, for a time-dependence $e^{-i\omega t}$, the solution is

$$\nabla^2\mathbf{E} = -\frac{\omega^2}{c^2}\left(1 + \frac{4\pi i\sigma}{\omega}\right)\varepsilon(\omega)\mathbf{E} \ . \tag{4.5}$$

This equation is in the form of the wave equation

$$\nabla^2\mathbf{E} = -\frac{\omega^2}{c^2}\varepsilon(\omega)\mathbf{E} \tag{4.6}$$

with the complex dielectric function

$$\varepsilon(\omega) = 1 + \frac{4\pi i\sigma}{\omega} \ . \tag{4.7}$$

For the high frequencies such as $\omega\tau >> 1$, the complex dielectric function becomes

$$\varepsilon(\omega) = 1 - \frac{{\omega_P}^2}{\omega^2} \tag{4.8}$$

where ω_P is the plasma frequency and given by

$${\omega_P}^2 = \frac{4\pi ne^2}{m} \ . \tag{4.9}$$

In the free carrier Drude Model, which can be used for photoexcited carriers in which the electrons excited to the conduction band where they can be considered as free, the dielectric function is given as [70]

$$\tilde{\varepsilon}(\omega) = \varepsilon_{eff}^{\infty} - \frac{{\omega_P}^2}{\omega^2 + \frac{i\omega}{\tau}} \tag{4.10}$$

where $\varepsilon_{eff}^{\infty}$ is the effective dielectic constant at high frequencies. One model to describe the effective dielectric constant is the Maxwell-Garnett theory which describes the effective dielectric constant only for conductive and doped semiconductive particles implanted in a dielectric layer [70].

In the Drude-Lorentz Model [70], the charge carriers are assumed as freely moving and bound to the atoms quasi-elastically. The photoexcitation causes excitation and oscillation. In this model, the dielectric funtion is depicted as

$$\tilde{\varepsilon}(\omega) = \varepsilon_{eff}^{\infty} - \frac{\omega_P^2}{\omega^2 - \frac{i\omega}{\tau}} - \sum_{m=1}^{M} \frac{\Omega_m^2}{\left(\omega^2 - \omega_m^2\right) + i\omega\Gamma_m} \qquad (4.11)$$

where ω_m is the resonance frequency, M is the number of resonances, Ω_m is the oscillator strength, Γ_m is the resonance width [70].

4.3. Experiment

The epitaxial nominally undoped GaAs samples were grown at 600 ^{o}C to a 1 μm effective layer thickness on top of a 650 μm thick SI-GaAs wafer. The resistivity measurements were done by the van der Pauw technique along with the standard Hall Effect measurements [56] to determine mobilities and the carrier concentrations. To obtain accurate data, very small (less than 1 mm^2) AuGe Ohmic contacts were devised at the corners of the square shaped (1.4 cm x 1.4 cm) GaAs sample. The resistivity, conductivity, Hall coefficient, charge carrier concentration, and mobility of the p-type GaAs samples were calculated to be 10.4 Ω.cm, 0.096 Ω.cm^{-1}, 5800 cm^3.C^{-1}, 1.1x10^{15} cm^{-3}, and 550 cm^2.V^{-1}.s^{-1} respectively.

The THz spectroscopy techniques, on the other hand, provide noncontact measurements with subpicosecond temporal resolution as an alternative method in the field of solid state electronics where it is difficult to use traditional probes. This makes THz spectroscopy an ideal tool for measuring the conductivities and obtaining data on charge carrier dynamics without use of electrical contacts.

The THz-TDS system used in these measurements was driven by a mode-locked Ti:Al_2O_3 laser (Femtosource) with a center wavelength of λ = 800 nm

and a pulse duration of τ = 15 fs at a repetition rate of 75 MHz. 180 mW of the average beam power is split into two optical lines, where 36 mW is fed through to a LT-GaAs based photoconductive antenna (PCA) (BATOP Optoelectronics GmbH) where a dipole gap of 6 μm is used for generation. The antenna bias was AC modulated by a function genetator at 2.5 kHz with $V_{p\text{-}p}$ = 10 V. For the detection of the THz beam, the electro-optic method is performed by use of a 2 mm thick <110> oriented ZnTe crystal, a quarter wave-plate (QP), Wollaston prism (WP) and a balanced photodetector. The amplitude and phase of the signal was detected with the aid of a digital dual channel lock-in amplifier (Stanford Instruments, Model SR830 DSP). The photoexcited measurements were made with the aid of 750 mW continuous laser power at 808 nm pump wavelength. The sample was placed at 45^{o} to the THz and the probe beam. The THz beam was focused on the sample by using 10 cm focal length TPX lenses. The system is illustrated in Figure 4.1.

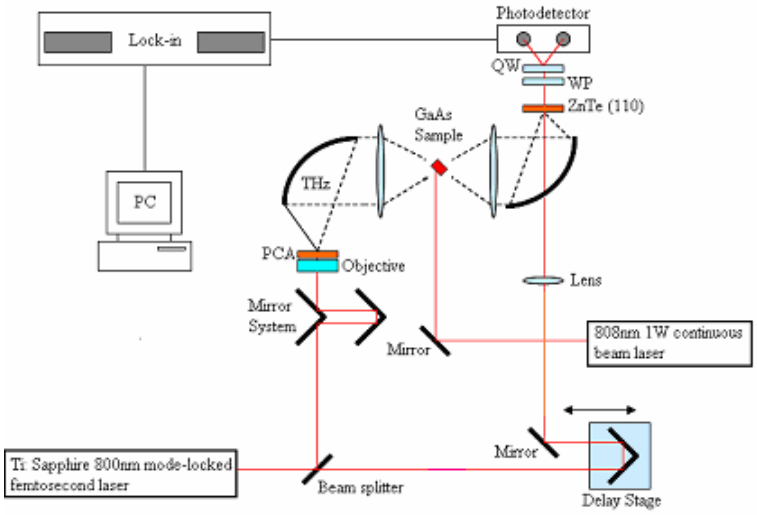

Figure 4.1: THz spectroscopy system for the probe measurements

The typical THz time-domain waveforms measured on the GaAs sample is shown in Figure 4.2. The Fast Fourier transforms of the THz time-domain data is shown Figure 4.3.

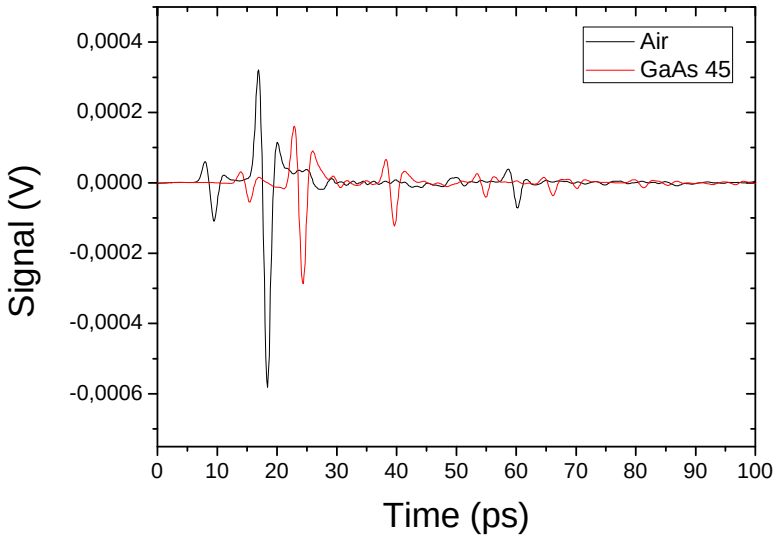

Figure 4.2: THz-TDS scan of the direct spectroscopy of GaAs compared with air.

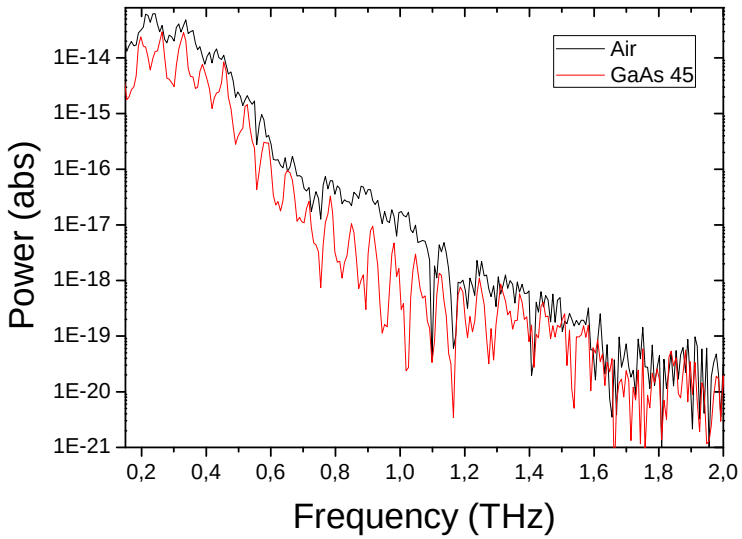

Figure 4.3: FFT of the direct spectroscopy of GaAs compared with air.

The photoexcited THz time-domain waveforms measured on the GaAs sample is shown in Figure 4.4. The Fast Fourier transforms of the photoexcited THz time-domain data is shown Figure 4.5.

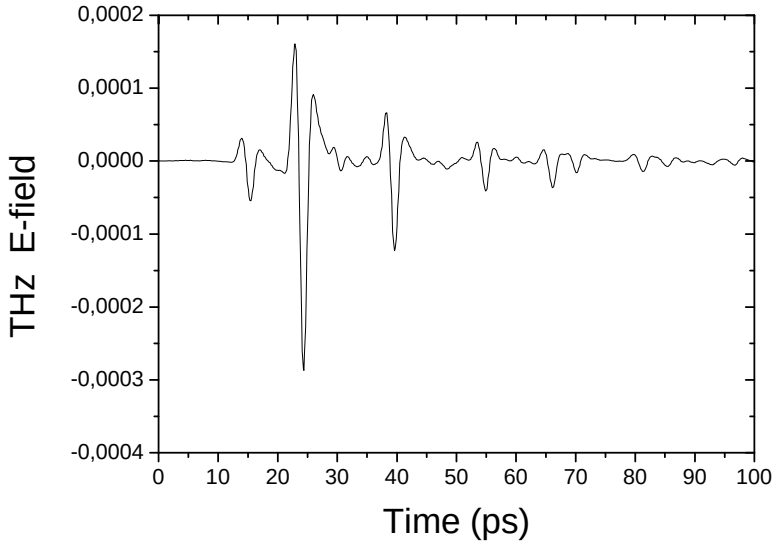

Figure 4.4: THz-TDS of Time-Domain scan of the photoexcited spectroscopy

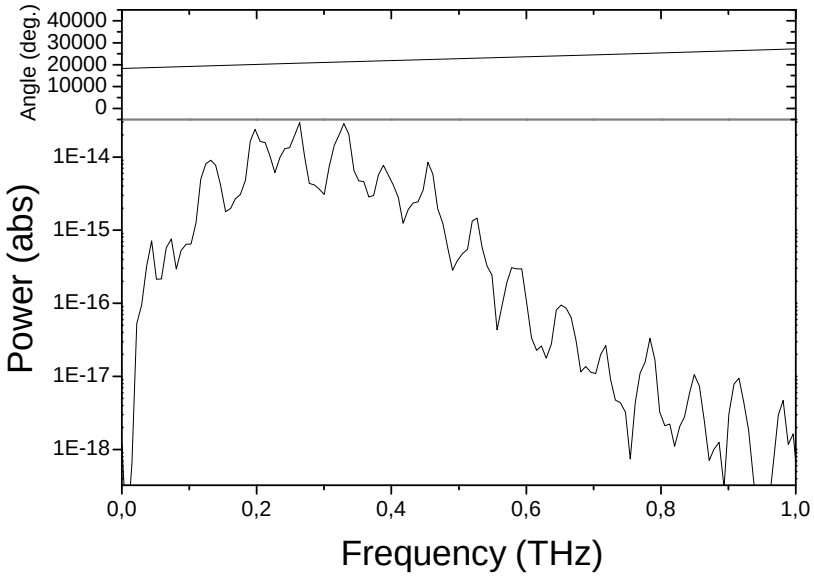

Figure 4.5: FFT of the photoexcited spectroscopy

4.4. Analysis

In the THz time-domain spectroscopy, the time-dependent THz electric field is measured and compared with the reference data. Both the amplitude and the phase of the Fast-Fourier Transform (FFT) components of the transmitted THz pulse are determined.

For the spectral analysis, Fast Fourier Transform (FFT) is applied to the time domain data and the resulting THz electric field is given by

$$E(\omega) = A(\omega)e^{i\varphi(\omega)} \tag{4.12}$$

where $A(\omega)$ and $\varphi(\omega)$ are frequency-dependent amplitude and phase, respectively.

Using the experimental data, the real (n_r) and complex (n_i) components of the refractive index can be calculated by

$$n_r = \frac{1}{kl}\left(\varphi(\omega,l) - \varphi(\omega)\right) \text{ and } n_i = \frac{1}{kl}\left(\ln\left(\frac{E(\omega,l)}{E(\omega)}\right)\right) \tag{4.13}$$

where k is the wave number, l is the thickness of the sample. The results of these calculations are shown in Figures 4.6.

The absorption coefficient of the sample can be obtained as

$$\alpha = \frac{1}{l}\left(\ln\left(\frac{I}{I_0}\right)\right) \tag{4.14}$$

where I is the intensity after transmission and I_0 is the intensity without sample.

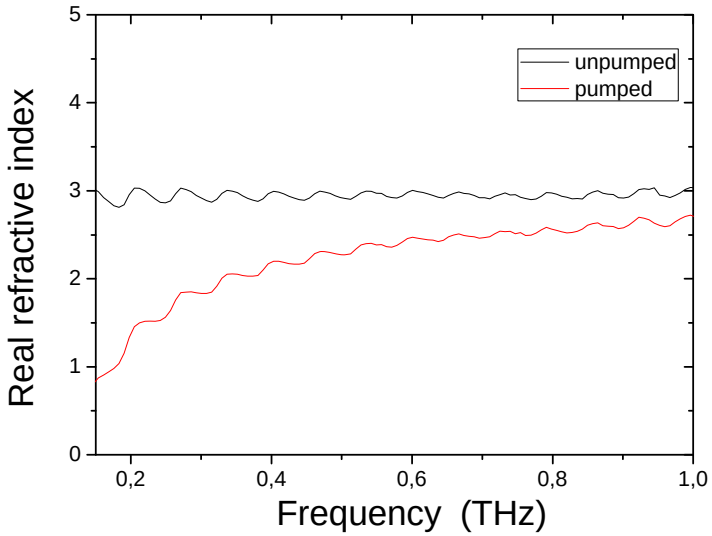

Figure 4.6: The real part of the refractive index obtained by direct (unpumped) and photoexcited (pumped) THz spectroscopy

The complex absorption spectrum is obtained by the Fourier analysis and the imaginary index is given by

$$\alpha = \frac{2n_i\omega}{c}. \tag{4.15}$$

Any of the above parameters can be obtained experimentally, however, the other carrier dynamics, such as conductivity and mobility can be extracted from an appropriate conduction model. In order to calculate the conductivity and the mobility, the Drude model for electrical conductivity is appropriate to use in which the charge carriers can move freely, although their motion is subject to damping with time constant τ. From the experimental values, the imaginary and real components of conductivity are calculated by

$$\sigma_i = \frac{\varepsilon_0 \omega \omega_p^2}{\omega^2 + \langle \tau \rangle^{-2}} \quad . \tag{4.16}$$

In this equation, the collision frequency is defined as $1/\tau = \nu_c$, and the plasma frequency is given by the relation

$$\omega_p = \left(\frac{Ne^2}{m\varepsilon_0} \right)^{1/2} , \tag{4.17}$$

where N is the number density, e is the charge of the free carriers, m is the mass of the free carriers. From this model, the Drude parameters for direct THz time- domain spectroscopy are calculated to be $N_p = 1.0 \times 10^{16}\, cm^{-3}$, $\upsilon_c = 5.26 \times 10^{12}\, s^{-1}$ where m_p^{*} = 0.45 m_0 [71] and for the photoexcited THz time-domain spectroscopy $N_n = 1.0 \times 10^{16}\, cm^{-3}$, $\upsilon_c = 8.33 \times 10^{13}\, s^{-1}$ where $m_n^{*} = 0.067\ m_0$.

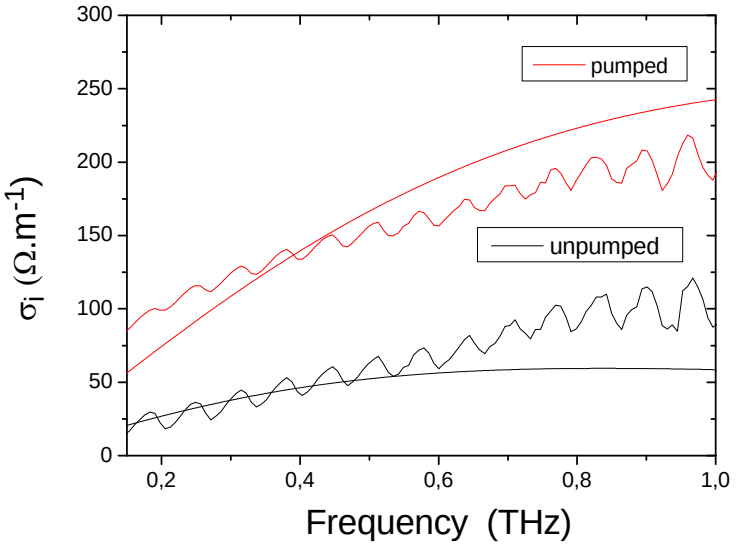

Figure 4.7: The conductivities obtained by direct (unpumped) and photoexcited (pumped) THz spectroscopy with their Drude fits

Hence, using the relation

$$\mu = \frac{e}{m\nu_c} \ , \tag{4.18}$$

the calculated mobility values of the GaAs sample from the direct and photo excitation measurements are 740 and 3150 $cm^2\ V^{-1}\ s^{-1}$, respectively.

4.5. Discussion

Main results of this chapter can be summarized as follows: The THz-TDS measurements allows a quick way of determining the real (n_r) and complex (n_i) components of the refractive index of material. We have demonstrated that direct and photoexcited THz-TDS measurements give an estimate of the carrier densities and both the hole and electron mobility values with good precision. In the photoexcited analysis, we have found the mobility value of the GaAs sample as 3150 $cm^2\ V^{-1}\ s^{-1}$ which may not be accurate, since in this calculation we assumed that the number density $N = 1.0 \times 10^{16} cm^{-3}$ does not change with the photoexcitation. We also assumed that only the 1 μm thick epitaxial layer makes the contribution to the results, not the semi-insulating layer. The reason for both of these assumptions is the low power and low photon flux of laser used in photoexcitation. However, the photoexcitation increases the number of collisions and the collision frequency. So, the Drude fit was determined from the collision frequency. For this reason, better approximation of experimental results should rely on both of the parameters. In addition, here, we assumed a single layer transmission in our calculations, inclusion of multilayer transmissions may improve the accuracy of the results. In addition, as can be seen from Figures 4.2, 4.3, 4.4, and 4.5, there are Fabry-Perot (etalon) oscillations in the time-domain and frequency domain. In Figure 4.2, the "etalon" peak comes 14.53 ps later than the main peak. In Figure 4.3, there are

"etalon" oscillations in the Fourier transformed spectra and these oscillations are approximately 0.07 THz apart. These "etalon" effects interfere with the transmission data and enters into the data analysis. Elimination of these "etalon" effects will also introduce an improvement to the data analysis. In the next chapter, we shall show how to avoid these unwanted "etalon" oscillations by using an algorithm.

In conclusion, while the Hall effect and van der Pauw measurements are more accurate, THz-TDS coupled with photoexcitation allows for measurement of electron mobilities of p-type epitaxial samples [77].

CHAPTER 5

NUMERICAL IMPROVEMENT OF TERAHERTZ TIME-DOMAIN SPECTROSCOPIC MEASUREMENTS

5.1. Introduction

We have developed an algorithm to eliminate efficiently the unwanted reflections typically observed in the data obtained by Terahertz time-domain spectroscopic (THz-TDS) methods. The algorithm works by eliminating the reflections from the boundaries. The numerical improvement of the data allows better analysis of the critical parameters obtained by THz-TDS systems.

5.2. Fabry-Perot Effect

Interference effects can cause multiple reflections in the time-domain spectroscopy systems [29]. This becomes problematic if the wavelengths are comparable with the sizes of the elements or samples used in the system. The reflections usually emerge from the surfaces of the samples under investigation or the crystals used in THz generation or THz detection processes. These are clearly visible in the time-domain data and in the Fourier transformed data.

In the time-domain data, these reflections are usually in the form of repetitions of the main THz peak but in lower amplitudes. For example, in Figure 5.1, the THz time-domain transmission data for 1 mm ZnTe <110> sample is shown. The etalon reflections of the main peak are clearly recognizable.

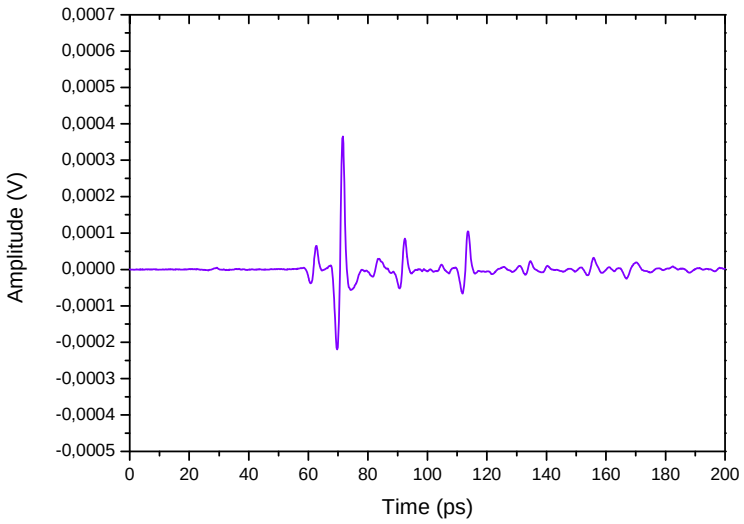

Fig.5.1. The THz time-domain data for the 1 mm ZnTe data

In the Fourier transformed data, they are in the form of periodic oscillations. Hence, when the material characteristics are obtained through THz spectroscopic analysis, these etalon effects should be taken into account in order to improve the spectral analysis. For example, in Figure 5.2, the Fourier transformed data up to 0.8 THz for the THz time-domain transmission data for 1 mm ZnTe <110> sample is shown. The etalon reflections of the main peak are seen in the form of small oscillations of the main FFT profile.

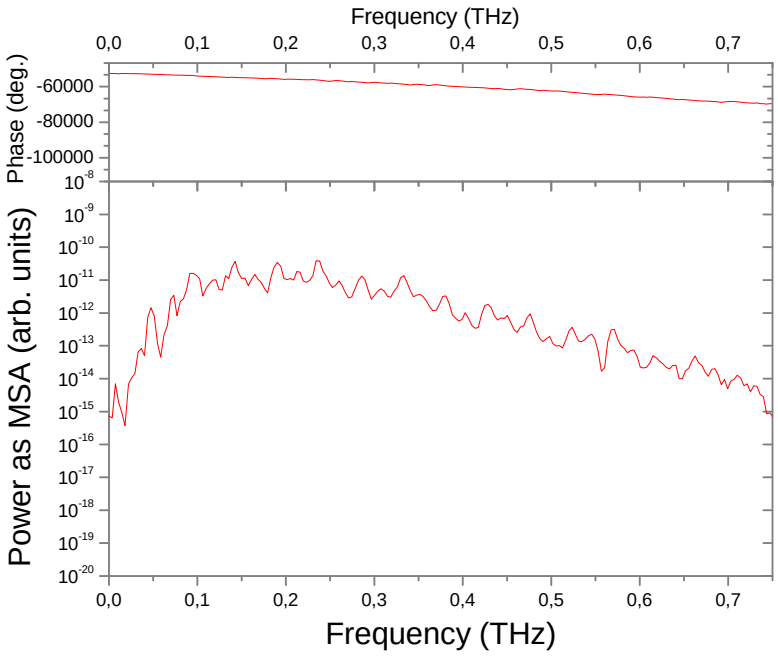

Fig.5.2. The THz FFT transformed data for the 1 mm ZnTe data
(MSA: Mean Square Amplitude)

5.3. The Algorithm

The aim is to eliminate the reflection peaks due to etalon effect while keeping the spectral information intact. There are several experimental techniques for avoiding the reflection coming from detection crystals such as anti-reflection coatings and attaching crystals with different orientation, for example ZnTe <100> in front of the ZnTe <110> detector [75, 76], since this <100> ZnTe crystal makes the reflection peak come much later. However, when it comes to the reflections coming from the samples under investigation, these techniques are inefficient [30].

As demonstrated previously by M. Naftaly *et al* [30], the THz-TDS data including these reflections can be simulated with the convolution of the main

THz peak and delta functions coinciding all the peaks in the spectrum. Here it is important to keep the resolution and the spectral data, so the algorithm is applied to the time-domain data and then to its Fast Fourier Transform (FFT) by manually choosing the secondary and other unwanted reflection peaks.

The algorithm, which is developed in MATLAB and given in Appendix, is based on approximating the time domain data by a delta function for each peak in the waveform. Afterwards, the FFT of the real data is divided by the FFT of the approximated waveform to get rid of the unwanted oscillations in the frequency domain data sets.

Time-domain Dirac Delta Function set amplitudes are given by

$$A(t) = A_o(t) \otimes \sum_{i=0}^{\infty} a_i \delta(t_i) \tag{5.1}$$

where i donates the number of the peak and a_i denotes amplitudes of each delta function, $A_0(t)$ is the normalization factor [30].

We assume our real data set is made up of the corrected data set and the Dirac function data set in frequency-domain:

$$E(\nu) = F\left|A(t)\right| = F\left|A_0(t)\right| \otimes F\left|\sum_i a_i \delta(t_i)\right| \tag{5.2}$$

From here we extract the corrected data set in the frequency domain

$$E_{corrected}(\nu) = F\left|A_0(t)\right| = E(\nu) \otimes \frac{M}{F\left|\sum_i a_i \delta(t_i)\right|} \tag{5.3}$$

Here, M is the normalizing factor equal to the mean value of the Fourier transform of the delta set.

The determination of the etalon peaks and the Dirac delta function sets is illustrated in Figure 5.3. Here the etalon reflections are determined manually first and then the algorithm written in MATLAB is executed. The program replaces each of the selected peaks with normalized Dirac delta function and removes the etalon peaks from the time-domain data.

We have successfully implemented this algorithm to the THz transmission data for the ZnTe crystals with different thicknesses and clearly observed that the oscillations are reduced without having any loss of information in the Fourier spectrum.

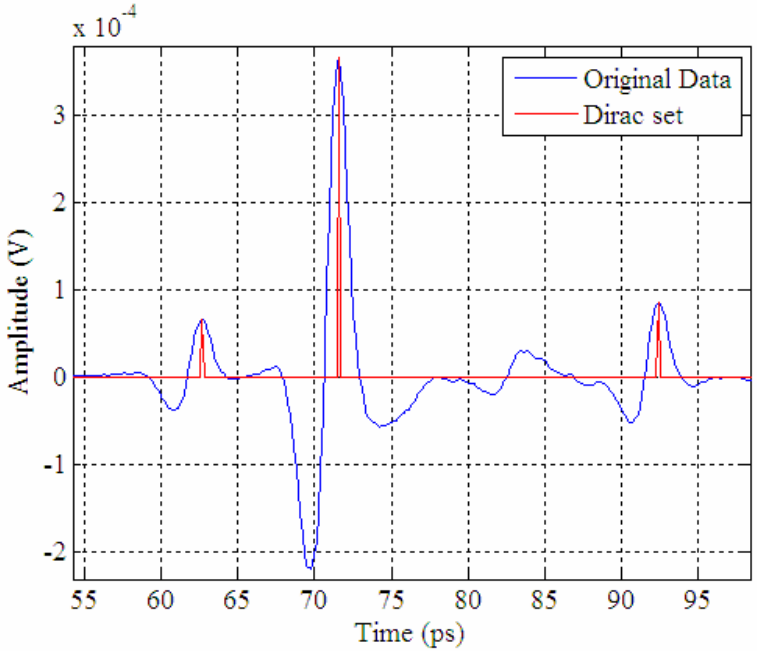

Fig.5.3. An example of the determination of etalon reflections and the implementation of the removal procedure

We observed that some THz absorption data that are not significant or lost in the real data due to the many oscillations become apparent after the implementation of the algorithm. The time-domain data for the 1 mm ZnTe <110> crystal after the implementation of the algorithm is shown in Figure 5.4. It is clearly seen from the comparison of Figures 5.1 and 5.4 that the algorithm provides a simple and practical way to remove the unwanted reflections which is very hard to eliminate experimentally.

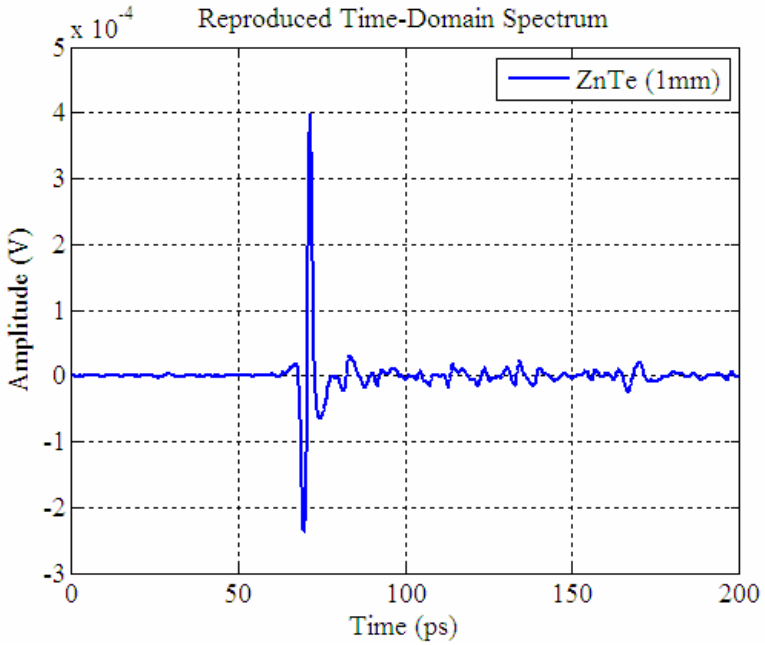

Fig.5.4. The THz time-domain spectrum after the implementation of the algorithm

5.4. Experiment

We performed THz-TDS measurements to study the “etalon” effects from the <110> oriented ZnTe crystals of known thicknesses. From the time-domain data, we determined where these the “etalon” reflections coming from. After

that we implemented the algorithm, which is given in Appendix A, to eliminate the “etalon” peaks.

The THz time-domain spectrometer used in these “etalon studies” is driven by a mode-locked Ti:Al_2O_3 laser with a center wavelength of λ = 800 nm and a pulse duration of τ = 30 fs at a repetition rate of 80 MHz. 180 mW of the average beam power is split into two optical lines, where 36 mW is fed through to a LT-GaAs based photoconductive antenna (PCA) with a dipole gap of 6 μm is used for generation. The antenna bias was AC modulated at 2.5 kHz with $V_{p\text{-}p}$ = 10 V. For the detection of the THz beam, the electro-optic method is performed by use of a 2 mm thick <110> oriented ZnTe crystal, a quarter wave-plate, Wollaston prism (WP) and a balanced photodetector.

The amplitude and phase of the signal was detected with the aid of a digital dual channel lock-in amplifier (Model SR830 DSP). The sample was placed perpendicular to the THz field. The THz beam was focused on the sample by using 10 cm focal length TPX lenses. The system is shown in Figure 5.5.

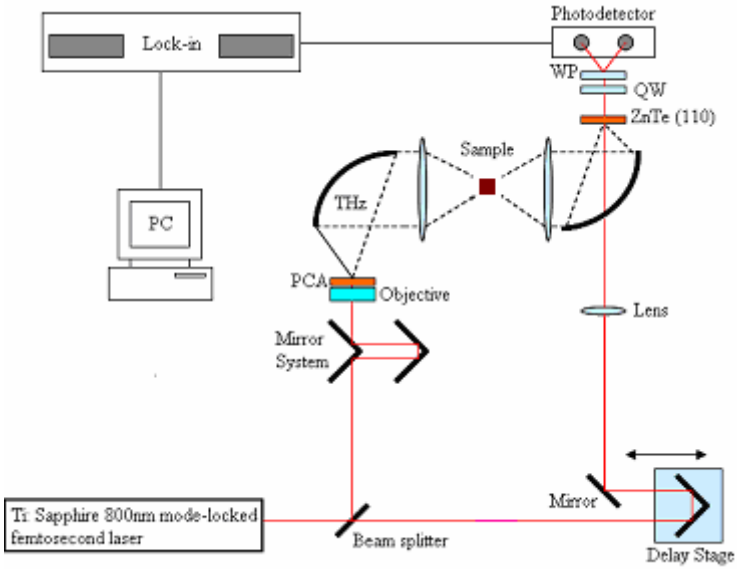

Fig.5.5. THz spectroscopy system for the transmission measurements

We performed THz transmission measurements on <110> oriented ZnTe crystals with 1 mm, 1.5 mm, and 2 mm thicknesses. The THz time-domain data for these crystals and the reference is shown in Figure 5.6.

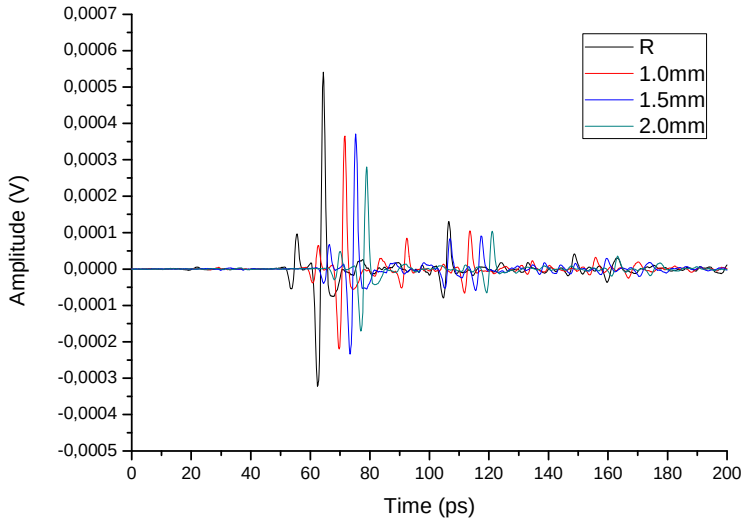

Fig.5.6. THz time-domain transmission data for the reference and 1.0 mm, 1.5 mm, 2.0 mm thick <110> ZnTe crystals

The etalon reflections for each of these measurements are presented in Figure 5.7. The reflection peaks in these measurements can be classified as follows: Gate-reflections (due to the probe beam in the THz detection process), reflections from the surfaces of the sample, and the reflections from the ZnTe crystal used in the detection arm. For the 1 mm thick crystal, as shown in Figure 5.7.b, the peak no.1 is due the gate reflection, no.2 is due to the reflection from the sample, no.3 from the sample and the detecting crystal, no.4 is from the sample again, and no.5 is from the sample and the detecting crystal. Although there exists experimental techniques [32] to eliminate these effects, numerical techniques are more practical.

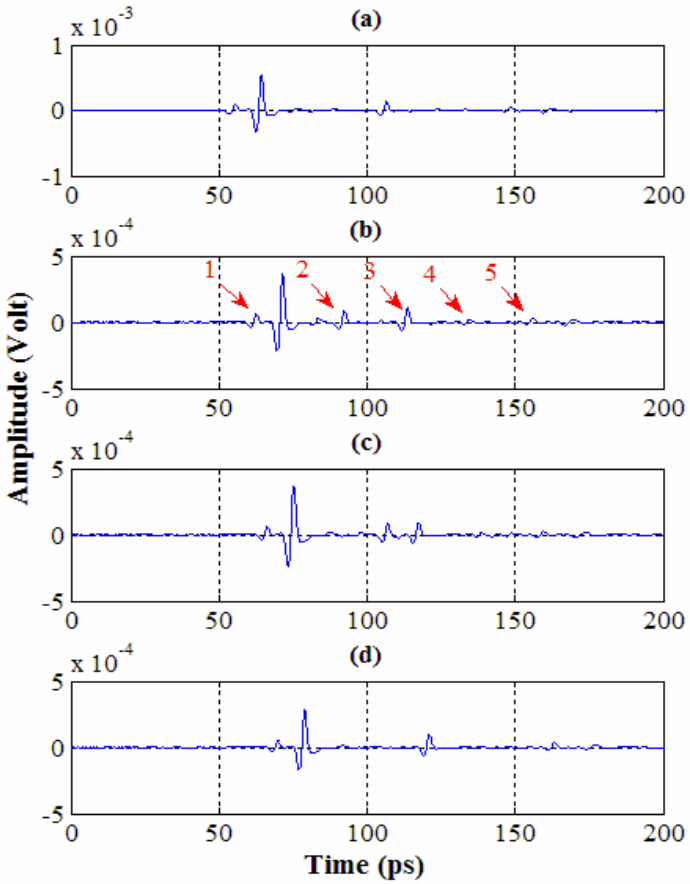

Fig.5.7. THz time-domain spectroscopic data for (a) reference and (b) 1 mm (c) 1.5 mm (d) 2 mm thick ZnTe <110> crystals sample.

We observe that some THz absorption data that are not significant or lost in the real data due to the many oscillations become apparent after the implementation of the algorithm as shown in Figure 5.8.

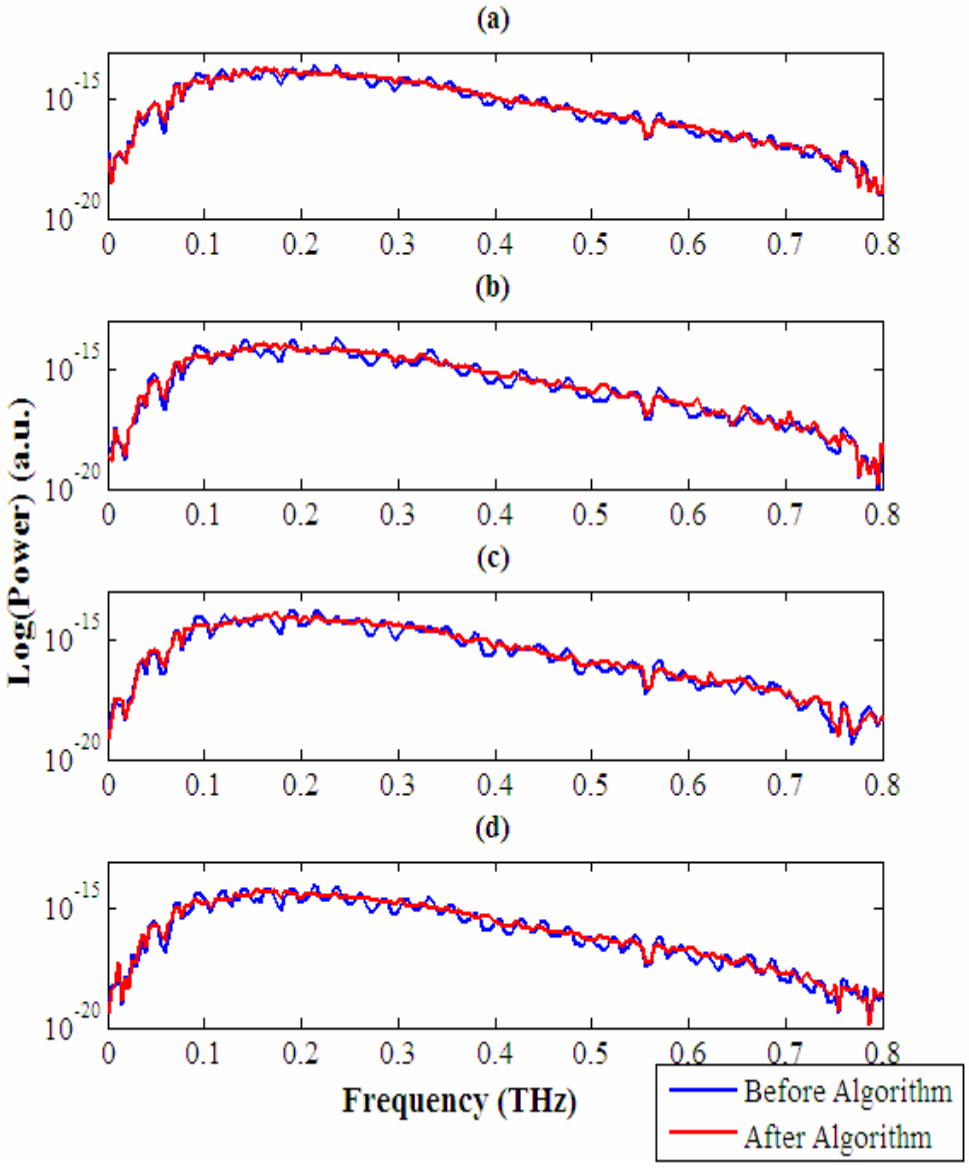

Fig.5.8. Fourier Transforms for (a) reference and (b) 1 mm (c) 1.5 mm (d) 2 mm thick ZnTe <110> crystals with and without algorithm.

If the sample is made of a material absorbing the THz radiation highly as a function of frequency, the algorithm should be applied very carefully to keep the spectral information, since absorption causes the secondary and other peaks

to become wider than the main THz peak in the time-domain data. This widening may include spectral data and hence cause the loss of information at higher frequencies. In the Fourier transformed data, this is realized by the decay of etalon oscillations at higher frequencies. In such a case, as suggested by M. Naftaly *et al.* [30], the algorithm is to be modified by adding an empirically generated dissipation funtion to the FFT of the delta functions. However, this extra procedure should be applied after the determination of the absorption characteristics from the comparison of the spectrum of the sample and that of reference, i.e. dry air. Then, it is possible to determine the dissipation funtion from the absorption curve [31].

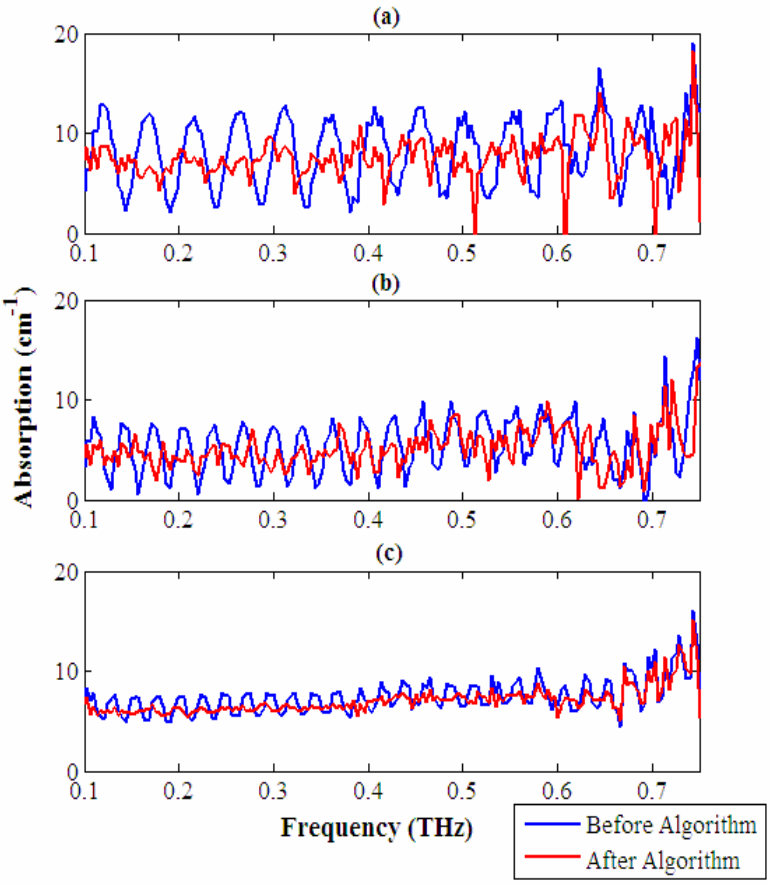

Fig.5.9. Absorption spectrum of (a) 1 mm (b) 1.5 mm (c) 2 mm thick ZnTe <110> crystal samples with and without the algorithm.

In summary, for samples of low dispersion and low absorption, the method shown above is effective. The dramatic reduction in the oscillations can be observed in the absorption spectrum shown in Figure 5.9, while the overall shape of the absorption is not affected. This algorithm serves as a robust and reliable tool in practice to improve the analysis of the data and offers promise for potential use in commercial applications of THz-TDS systems.

5.5. Frequency Calibration Test using the Etalon Model

One can use the "etalon effect" to verify the frequency resolution of the THz-TDS system. In this part of "Etalon study", the time-domain data for 1mm <110> ZnTe is used with the Etalon Model to check the frequency calibration of the system used in this thesis.

As stated before, in THz time-domain spectroscopy, the spectrum in the frequency domain is calculated numerically by Fast Fourier Transform (FFT). For this reason, all the experimental errors, including the etalon reflections, are transformed into the FFT data. However, the "etalon reflections" from a smooth surface, terahertz transparent material with known thickness, can be implemented to get the calibration degree of the THz spectroscopy system. Since these "etalon reflections" show themselves in the form of periodic oscillations in the frequency domain, so the matching between the "modeled etalon oscillations" and the experimentally obtained data provides a method to qualify the calibration of the THz spectrometer system.

In this Etalon Model [31, 32], the transmission spectra as a function of frequency is given by

$$T = \left(1 + \frac{4R}{(1-R)^2}\sin^2\frac{\delta}{2}\right)^{-1} \tag{5.4}$$

In this equation,

$$R = \left(\frac{n(f)-1}{n(f)+1} \right)^2 \text{ and } \delta = {4\pi n(f) l f}/{c} \tag{5.5}$$

where l is the thickness and c is the speed of light [32].

The calculated values of etalon peaks and troughs enables the calibration technique. Here, we calculated the index of refraction from the terahertz spectropic methods namely, since the THz power is quite low, we assumed the interaction of THz pulse and the sample as linear. The index of refraction then is calculated from the formula

$$n_r = \frac{1}{kl}\left(\varphi(\omega, l) - \varphi(\omega)\right) \tag{5.6}$$

This technique is applied for the 1mm ZnTe <110> crystal. The peaks calculated from the model and the peaks measured from the experiment were compared with each other in the frequency domain as shown in Figure 5.10.

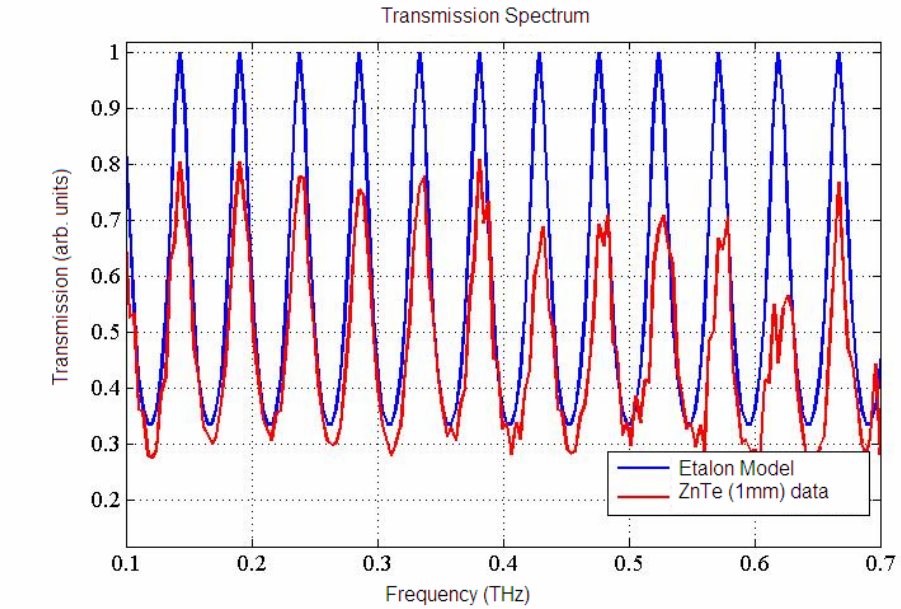

Fig.5.10. Transmission spectrum on 1mm thick ZnTe and the "etalon" model

In performing these experiments, we made a scan of 30 mm corresponding to 200 ps of time-domain data, and the resulting observed shift was 5 to 10 GHz in the transmission spectra.

5.6. Discussion

In THz time-domain spectroscopy systems, the Fabry-Perot reflection from the optical elements used in the system introduced unwanted experimental problems. The experimental techniques such as coating or filters, brings extra difficulty and generally difficult to perform. Implementation of an algorithm which is based on the theoretical determination of these “etalon” reflections, on the other hand, provides a simple way to improve the quality of the spectroscopic analysis. We have here demonstrated that the usage of such algorithm is effective. The experimental results from the Terahertz transmission measurements of 1.0 mm, 1.5 mm, and 2.0 mm ZnTe <110> crystals were also analyzed with the algorithm applied data. From the measurements, it’s also demonstrated that these “etalon” reflections can also be used to check the frequency calibration check. Since the THz powers of the spectrometers is quite low, we have assumed that our system is linear. For this reason, we calculated the thickness of the samples from the THz data and used this thickness in calculation of frequency calibration. Better determination of sample thickness provides better calibration check.

CHAPTER 6

CONCLUSION

In this thesis, we have performed terahertz time-domain spectroscopic measurements for material characterization. To do that, we have constructed different terahertz spectrometers and optimized them for system performance. This task turned out to be directly related to the ultra-fast lasers used in the spectrometers, since the pulse profile of the laser affects the terahertz profile and power.

Among the different spectrometer configurations previously described in chapter two, we preferred the one based on photoconductive generation and electro-optical sampling for detection. The photoconductive antennas provide more power than the optical rectification. In addition, it requires less laser power (~35-36 mW at ~800 nm) with compared to the optical rectification. So, the femtosecond fiber lasers which are compact, robust and low-cost can be used for that purpose. The disadvantage of photoconductive antennas is in alignment problems and narrow bandwidth. For the detection of terahertz radiation, the electro-optic sampling is advantageous, since its detection bandwidth is broader, sensitivity is higher, and the alignment is easy.

The terahertz time-domain spectrometer mentioned above were tested and optimized for characterization of wide-band-gap and semiconductor crystalline materials. It was used in the study of the carrier dynamics of MBE grown

nominally undoped epitaxial GaAs samples and the terahertz transmission studies of isotropic ZnTe <110> crystal of different thicknesses. In addition to the standard time-domain measurements, photoexcited dynamics of the epitaxial GaAs samples were also investigated. The measurements were done in a class 10000 clean room under room temperature. The reference data were taken before and after each measurement to check the optimization and consistency of the spectrometer system. It was shown that THz-TDS coupled with photoexcitation allows for measurement of electron and hole mobilities of p-type epitaxial samples [77].

THz-TDS measurements for nominally undoped epitaxial GaAs samples were analyzed according to the spectropic analysis technique outlined in the chapter two. The calculation were done under the assumptions of the Drude model. From this model, the Drude parameters for the direct (unpumped) THz-TDS were calculated. These were the charge carrier concentration, which is found to be $N = 1.0 \times 10^{16} cm^{-3}$ and the collision frequency is $\upsilon_c = 5.26 \times 10^{12} s^{-1}$. On the other hand, the photoexcited (pumped) THz-TDS were also performed by using a continuous beam laser of λ = 808 nm. From these measurements, the charge carrier concentration is again calculated to be $N = 1.0 \times 10^{16} cm^{-3}$, whereas the collision frequency is found to be as $\upsilon_C = 8.33 \times 10^{13} s^{-1}$. The photoexcitation caused a drastic increase in the carrier concentration. From these results, the calculated the mobility values of the GaAs sample from the direct (unpumped) and photoexcitated (pumped) data are 740 $cm^2\ V^{-1}\ s^{-1}$ and 3150 $cm^2\ V^{-1}\ s^{-1}$ respectively. Here the mobility of the photoexcited GaAs sample may not be accurate, since the Drude fit was determined from the collision frequency while assuming the number density does not change with the photoexcitation. However, better approximation of experimental results should rely on both of the parameters. On the other hand, inclusion of multilayer transmissions may also improve the accuracy of the results.

The results from terahertz studies were compared with the electrical characterization of the GaAs samples. From the Hall effect measurements coupled with van der Pauw technique, their room temperature resistivities of the MBE-grown GaAs samples was found to be 10.385 Ω.cm. The samples were of 1μm thickness and their conductivities were calculated to be 0.096 $\Omega^{-1}.cm^{-1}$. Their Hall coefficients were 5750 $cm^3.C^{-1}$ with a charge carrier concentration of $1.09x10^{15}$ cm^{-3}. The mobility of the samples were found to be 553.68 $cm^2.V^{-1}.s^{-1}$.

It was shown that the THz-TDS measurements allow a quick way of determining the real and complex components of the refractive index of the material. On the other hand, for the determination of mobility and majority carrier density, it was found that the Hall effect measurements coupled with the van der Pauw technique was led to more accurate results even though there exists problems due to electrical contacts, wiring, etc.

In this thesis, a commonly encountered problem of Fabry-Perot reflections emerging from the optical elements and samples used in the experiments were also studied in the scope of the formalism of suggested by M. Naftaly, *et al.* [30, 31]. An algorithm was developed (see Appendix A) for elimination of these "etalon" effects from the time-domain data. This was further demonstrated by the experimetal application of this technique to ZnTe <110> crystals of different thicknesses. We found that the algorithm provides a numerical improvement to the analysis of the time-domain and Fourier transformed spectral data, since during the measurements the Fabry-Perot oscillations interfere with the time-domain data and effecting the analysis. On the other hand, this unwanted "etalon" effect was used to check the frequency calibration of the terahertz time-domain spectrometer used in this analysis, we have found that a scan of 30 mm corresponding to 200 ps of time-domain data, and the resulting observed shift was 5 to 10 GHz in the transmission spectra [78].

The majority carrier dynamics of the materials used in the production of terahertz generation and detection antennas is of crucial importance. Since the emitted terahertz bandwith and power is quite low even though the signal-to-noise is good. In order to increase the bandwidth and power, new materials for antenna production needs to be investigatied. In this sense, this thesis provides a methodology for analyzing direct gap semiconductor materials which can be implemented into the terahertz generation and detection. With the invention of new antenna materials and design, the terahertz research will be enhanced. Especially, high powers obtained will provide better transmission and broader bandwith provide more spectral information. Both of these in turn will lead to terahertz spectroscopic systems capable of remote sensing, imaging and spectral analysis, at the same time. The developments in the ultra-fast laser technologies, on the other hand, will lead to better terahertz profiles and faster time-gating. In addition, these will lead to transportable compact terahertz systems which can be implemented in to home-land security applications.

REFERENCES

1. Siegel, P.H., "*Terahertz Technology*", IEEE Transactions on Microwave Theory and Techniques, **50**, 910-928, (2002)
2. Auston, D.H., Cheung, K.P., and Smith, P.R., "*Picosecond Photoconductive Hertzian Dipoles*", Applied Physics Letters, **45**, 284-286 (1984)
3. Darrow, J.T., Hu, B.B., Zhang, X.-C, and Auston, D.H., "*Subpicosecond electromagnetic pulses from large-aperture photoconductive antennas*", Optics Letters, **15**, 323–325 (1990)
4. Hu, B.B., et al, "*Optically steerable photoconductive antennas*", Applied Physics Letters, **56**, 886-888 (1990)
5. Shen, Y.C., Upadhya, P.C., Linfield, E.H.,Beere, H.E., and Davies,A.G."*Terahertz generation from coherent optical phonons in a biased GaAs photoconductive emitter*", Physical Review B, **69**, 225-235 (2004)
6. Baas, M., et al, "*Optical Rectification*", Physical Review Letters, **9**, 446-448 (1962)
7. Yang, K., Richards, L.P., and Shen, R.Y., "*Generation of Far-Infrared Radiation of Picosecond Light Pulses in $LiNbO_3$*", Applied Physics Letters, **19**, 320-323 (1971)
8. Auston, D.H., "*Cherenkov Radiation from Femtosecond Optical Pulses in Electro-Optic Media*", Physical Review Letters, **53**, 1555-1558 (1984)
9. Morris, J.R. and Shen, Y.R., "*Far-infrared generation by picosecond pulses in electro-optical materials*", Optics Communications, **3**, 81–84 (1971)

10. Shen, Y.R., "*Far-infrared generation by optical mixing*", Progress in QuantumElectronics, **4**, 207–232 (1976)
11. Kleinman, D.A. and Auston, D.H., "*Theory of electrooptic shock radiation in nonlinear optical media*", IEEE Journal Quantum Electronics, **20**, 964–970 (1984)
12. Auston, D.H., and Nuss, M.C., "*Electrooptic generation and detection of femtosecond electrical transients*". IEEE Journal of Quantum Electronics, **24**, 184–197 (1998)
13. Xu, L., Zhang, X.-C., and Auston, D.H., "*Terahertz beam generation by femtosecond optical pulses in electro-optic materials*", Applied Physics Letters, **61**, 1784–1786 (2000)
14. Ding, Y.J., "*Quasi-single-cycle terahertz pulses based on broad-band phase-matched difference-frequency generation in second-order nonlinear medium: High output powers and conversion efficiencies*" IEEE Journal of Selected Topics in Quantum Electronics, **10**, 1171–1179 (2004)
15. Wu, Q. and Zhang, X.-C., "*Free-Space Electro-Optic Sampling of Terahertz Beams*", Applied Physics Letters, 67, 3523-3525 (1995)
16. Jepsen, P.U., Winnewisser, C., Shall, M., Schya,V., Keiding, S.R., and H. Helm, H., "*Detection of THz pulses by phase retardation in lithium tantalite*", Physical Review E, **53**, 3052–3054 (1997)
17. Nahata, A., Weling, A.S., and Heinz, T.F., "*A wideband coherent terahertz spectroscopy system using optical rectification and electro-optic sampling*", Applied Physics Letters, **69**, 2321–2322 (1996)
18. Grischkowsky, D, Keiding, S., van Exter, M. and Fattinger, Ch., "*Far-infrared time-domain spectroscopy with terahertz beams of dielectrics and semiconductors*", J. Opt. Soc. Am. B, **7**, 10 (1990)
19. Li, M., Cho, G.C., Lu, T.-M., Zhang, X.-C., Wang, S.-Q., and Kennedy, J.T., "*Time-domain dielectric constant measurement of thin film in GHz–THz frequency range near the Brewster angle*", Applied Physics Letters, **74**, 2113–2115 (1999)

20. Hu, B.B., Nuss, M.C., "*Imaging with Terahertz Waves*", Optics Letters, **20**, 1716-1719 (1995)
21. K. Wynne and D. A. Jaroszynski, "*Superluminal terahertz pulses*", Optics Letters, **24**, 25–27, 1999.
22. Chen, Q. and Zhang, X.-C., "*Semiconductor dynamic aperture for near-field terahertz wave imaging*", IEEE Journal of Selected Topics in Quantum Electronics, **7**, 608–614 (2001)
23. van der Valk, N.C.J. and Planken, P.C.M., "*Electro-optic detection of subwavelength terahertz spot sizes in the near field of a metal tip*", Applied Physics Letters, **81**, 1558–1560 (2002)
24. Mittleman, D.M., et al., "*T-Ray Tomography*", Optics Letters, **22**, 904-906 (1997)
25. Ferguson, B., Wang, S.H., Gray, D., Abbot, D., and Zhang, X.-C. "*T-ray computed tomography*", Optics Letters, **27**, 1312–1314 (2002)
26. Han, P.Y., Cho, G.C., and Zhang, X.-C., "*Time-domain transillumination of biological tissues with terahertz pulses*", Optical Letters, **25**, 242-244 (2000)
27. Cheville, R.A. and Grischkowsky, D.R., "*Time-Domain Terahertz Impulse Ranging Studies*", Applied Physics Letters, **67**, 1960-1962 (1995)
28. Liu, H.B., Zhong, H, Karpowicz, N. ,Chen, Y. and Zhang, X.-C., "*Terahertz Spectroscopy and Imaging for Defense and Security Applications*", Proceedings of the IEEE, **95**, (2007)
29. Dorney, D.D., Baraniuk, R.G., and Mittleman, D.M., "*Material parameter estimation with terahertz time-domain spectroscopy*", Journal of Optical Society of America - A, **18**, (July 2001)
30. Naftaly, M., Miles, R.E., "*A method for removing etalon oscillations from THz time-domain spectra*", Optics Communications, **280**, 291-295 (2007)
31. Naftaly, M., et al., "*Frequency calibration of terahertz time-domain spectrometer*", Journal of Optical Society of America - B, **26**, (2009)

32. Krausz, F., et al. "*Femtosecond Solid-State Lasers*", IEEE Journal of Quantum Electronics, **28**, (1992)
33. Fermann, M.E., Galvanauskas, A., Sucha, G., Harter, D. "*Fiber-lasers for ultrafast optics*" Appl. Phys. B, **65**, 259-275 (1997)
34. Fermann, M.E., Hartl, I., "*Ultrafast Fiber Technology*", IEEE Journal of Selected Topics in Quantum Electronics, **15**, (2009)
35. Moulton, P.F., "*Spectroscopic and laser characteristics of Ti:Al_2O_3*", J. Opt. Soc. Am. B, **3**, (1986)
36. Femtolasers, "*Mirror-dispersion-controlled Ti:Sapphire Ocillator: Femtosource*", (2004)
37. Femtolasers, "*Dispersion Minimized Autocorrelator: Femtometer*", (2004)
38. Szipöcs, R., Ferencz, K., Spielmann, Ch., and Krausz, F., "*Chirped multilayer coatings for broadband dispersion control in femtosecond laser*", Optics Letters, **19**, 201-203 (1994)
39. Stigl, A. and Lenzner, M., Spielman, Ch., Szipöcs, R., and Krausz, F., "*Sub-10-fs mirror-dispersion-controlled laser*", Optics Letters, **20**, 602-604 (1995)
40. Spielman, Ch., Curley, P.F., Brabec, T., and Krausz, F., "*Ultrabroadband femtosecond lasers*", IEEE Journal of Quantum Electronics, **30**, 1110-1114, (1994)
41. Kogelnik, H.W., Irpen, E.P., Dienes, A., and Shank, C.V., "*Astigmatically compensated cavities for CW dye lasers*", IEEE Journal of Quantum Electronics, **8**, 373-379, (1972)
42. Sala, K.L., Kennedy-Wallace, G.A., and Hall, G.E., "*CW autocorrelation measurement of picosecond laser pulses*", IEEE Journal of Quantum Electronics, **16**, 990-996, (1980)
43. Diels, J.C.M., Fontaine, J.J., McMicheal, I.C., and Simoni, F., "*Control and measurements of ultrashort pulse shapes (in amplitude and phase) with femtosecond accuracy*", Appl. Opt., **24**, 1270 (1985)

44. Young, M., "Optics and Lasers: Including Fibers and Optical Waveguides", Springer (2000)
45. Hecht, J., "The Laser Guidebook", McGraw-Hill Professional (1999)
46. Kono, S., Tani, M., and Sakai, K., "*Generation and Detection of Broadband Pulsed Terahertz Radiation*", K. Sakai (Ed.): Terahertz Optoelectronics, Topics Appl. Phys., **97**, 31–64 (2005)
47. Reimann, K, "*Table-top sources of ultrashort THz pulses*", Rep. Prog. Phys. **70**, 1597-1632, (2007)
48. Lee, Y.S., "Generation and Detection of Broadband Terahertz Pulses", Springer, (2009)
49. Han, P.Y., Zhang, X-C., "*Free-space coherent broadband terahertz time-domain spectroscopy*", Meas. Sci. Technol., **12**, 1747–1756, (2001)
50. Nahata, A., Weling, A.S., and Heinz, T.F., "*A wideband coherent terahertz spectroscopy system using optical rectification and electro-optic sampling*", Applied Physics Letters, **69**, 2321–2322 (1996)
51. Dexheimer, S.L., "Terahertz Spectroscopy: Principles and Applications", CRC Press, (2008)
52. Nishizawa, S., et al., "*Terahertz Time-Domain Spectroscopy*", K. Sakai (Ed.): Terahertz Optoelectronics, Topics Appl. Phys., **97**, 203–271 (2005)
53. Schmuttenmaer, C.A., "*Exploring Dynamics in the Far-Infrared with Terahertz Spectroscopy*", Chem. Rev., **104**, 1759-1779 (2004)
54. van Exter, M., Grischkowsky, D.R., "*Characterization of an Optoelectronic Terahertz Beam System*", IEEE Transactions on Microwave Theory and Techniques, **38**, (1990)
55. Dorney, T.D., Baranjuk, R.G., Mittleman, D.M., "*Material parameter estimation with terahertz time domain spectroscopy*", J. Opt. Soc. Am. A, **18**, (2001)
56. ASTM International, "*Standard Test Methods for measuring Resistivity and Hall Coefficient and Determining Hall Mobility in Single-Crystal Semiconductors*", F 76 – 86, (2002)

57. van der Pauw, L.J., "*A method of measuring the resistivity and Hall coefficient on lamellae of arbitrary shape*", Philips Technical Review, **20**, 220-224 (1958)
58. van der Pauw, L.J., "*A method of measuring specific resistivity and Hall effect of discs of arbitrary shape*", Philips Res. Repts,.**13**, 1-9 (1958)
59. Putley, E.H, "Hall Effect and Related Phenomena". Butterworths, London (1960)
60. Hall, E.H., "*On a New Action of the Magnet on Electrical Current*", Amer. J. Math., **2**, 287-292 (1879)
61. M.C. Beard, G.M. Turner, and C.A. Schmuttenmaer, "T*ransient photoconductivity in GaAs as measured by time-resolved terahertz spectroscopy*", Phys. Rev. B, **62**, 15764-15777 (2000)
62. D. Grischkowsky, S. Keiding, M. van Exter, and C. Fattinger, "*Far-infrared time-domain spectroscopy with terahertz beams of dielectrics and semiconductors*", Journal of the Optical Society of America B: Optical Physics, **7** (10), 2006-20015 (1990)
63. M. van Exter, D. Grischkowsky, "*Characterization of an optoelectronic terahertz beam system*", IEEE Transactions on Microwave Theory and Techniques, **38** (11), 1684-1691 (1990).
64. M. van Exter, D. Grischkowsky, "*Optical and electronic properties of doped silicon from 0.1 to 2.0 THz*", Applied Physics Letters, **56** (17), 1694-1696 (1990)
65. M. van Exter, D. Grischkowsky, "*Carrier dynamics of electrons and holes in a moderately doped silicon*", Physical Review B, **41** (7), 12140-12149 (1990)
66. M. Hangyo, T. Nagashima, and S. Nashima, "*Spectroscopy by pulsed THz radiation*", Meas.Sci.Technol., **13**, 1727-1738 (2002)
67. G. Zhao, R.N. Schouten, N. van der Valk, W. T. Wenckebach, and P.C.M. Planken, "*Design and performance of a THz emission and detection setup based on a semi-insulating GaAs emitter*", Review of Scientific Instruments, **73** (4), 1715-1719 (2002)

68. Masahiko Tani, Shuji Matsuura, Kiyomi Sakai, and Shin-ichi Nakashima, "*Emission characteristics of photoconductive antennas based on low-temperature-grown GaAs and semi-insulating GaAs*", Applied Optics, **36**, 7853-7859 (1997)
69. Achcroft, N.W., Mermin, D.N., "Solid State Physics", Saunders College Publishing, (1976)
70. Altan, H., "Characteristics of Nanocomposites and Semiconductor Heterostructure Wafers Using THz Spectroscopy", PhD. Thesis, NJIT (2005)
71. Tobias Bauer, Johanna S. Kolb, Ernst Mohler, Hartmut G. Roskos, and Klaus Köhler, "*Terahertz optical properties of thin doped contact layers in GaAs device structures*", Semicond. Sci. Techol., **18**, 28-32, (2003)
72. van Exter, M. and Grischkowsky, D., "*Optical and electronic properties of doped silicon from 0.1 to 2 THz*", Appl. Phys. Lett., **56** (17), 1694-1696 (1990)
73. Grischkowsky, D., Keiding, S., van Exter, M., and Fattinger, C., "*Far-Infrared Time-Domain Spectroscopy with Terahertz Beams of Dielectrics and Semiconductors*", JOSA-B, **7**, 2006-2015 (1990)
74. Jeon, T., and Grischkowsky, D., "*Characterization of Optically-Dense, Doped Semiconductors by Reflection THz Time-Domain Spectroscopy*", Appl. Phys. Lett., **72**, 3032-3034 (1998)
75. J. Kröll, J. Darmo, K. Unterrainer, "*High performance of terahertz electro-optic detector*", Electron. Lett. **40**, 1879-1884 (2004)
76. Turchinovich, D. and J.I. Dijkhuis, J.I., "*Performance of combined <100>–<110> ZnTe crystals in an amplified THz time-domain spectrometer*", Optics Communications, **270**, 96-99, (2007)
77. Köseoğlu, D., Güllü, H.H. , and Altan, H., "T*Hz Probe Studies of MBE Grown Epitaxial GaAs*" {Electron Dynamics in Semiconductors, Optoelectronics and Nanostructures, Journal of Physics: JPCS, **193**, 012088 (2009)}

78. Köseoğlu, D., Berberoğlu, H. , and Altan, H. "*Numerical Improvement of Terahertz Time-Domain Spectroscopic Measurements*" {Proceedings of TERA-MIR 2009: NATO Advanced Research Workshop on Terahertz and Mid-Infrared Radiation: Basic Research & Practical Applications, November 2009}

APPENDIX A

NUMERICAL IMPROVEMENT SOFTWARE

The algorithm for eliminating “etalon” effects is written in MATLAB. It is given below:

```
fprintf(1,'Please write the name of file\n');
fprintf(1,'For example, filename.txt\n');
namedata = input(' ','s');
rawdata = load(namedata);
timeps = rawdata(:,1);
curns = rawdata(:,2);
dim = length(timeps);
figure(1),hold on
plot(timeps,curns,'Linewidth',2), grid on
title('Original Time-Domain Spectrum')
xlabel('Time (ps)')
ylabel('Amplitude (V)')
xy = [];
nn = 0;
disp('Right mouse button picks last point.')
but = 1;
```

```
while but == 1
    [xi,yi,but] = ginput(1);
    plot(timeps,curns,'-
',xi,yi,'ro','MarkerSize',8,'Linewidth',1)
    title('Original Time-Domain Spectra')
    xlabel('Time (ps)')
    ylabel('Amplitude (V)')
    hold on, grid on
end
xy = sort(xy(1,:));
s1 = size(xy);
np = s1(2);
m1 = max(curns);
for ii = 1:np
ind = abs(xy(1,ii)-timeps);
min1 = min(ind);
minx = find(min1==ind);
pks(ii) = max(curns(minx-15:minx+15));
loc(ii) = find(pks(ii)==curns);
end
diracset = zeros(dim,1);
diracset(loc) = pks;
figure(2)
plot(timeps,curns,timeps,diracset), grid on
legend('Original Data','Dirac set')
title('Time-Domain Spectra')
xlabel('Time (ps)')
ylabel('Y(t)')
L=length(curns);
NFFT = 2^nextpow2(L);
Y = fft(curns,NFFT)/L;
```

```
Y2 = fft(diracset,NFFT)/L;
dx=timeps(3)-timeps(2);
f = linspace(timeps(1),1/dx/2*(1-1/L),NFFT/2);
norm1=abs(Y(1:NFFT/2));
norm2=abs(Y2(1:NFFT/2));
norm1 = norm1.^2/NFFT;
norm2 = norm2.^2/NFFT;
normx = norm1./norm2;
meandirac = mean(norm2);
figure(4)
act = meandirac*normx;
semilogy(f,norm1,f,act,'-r','Linewidth',1), grid on
legend('Before Algorithm','After Algorithm')
axis([0 2.5 1e-22 1e-12])
title('Fourier transform of THz Time-Domain Spectra')
xlabel('Frequency (THz)')
ylabel('|Y(f)|^2')
figure(5)
pha2 = unwrap(angle(Y2));
pha = unwrap(angle(Y));
pham = -pha(1:NFFT/2)*180/pi + pha(1)*180/pi;
phanewx = pha-pha2;
plot(f,pham), grid on
xlabel('Frequency (THz)')
ylabel('Unwrap Phase (Degree)')
figure(6)
semilogy(f,norm1,f,act/100,'-r','Linewidth',1)
legend('Before Algorithm','After Algorithm')
xlabel('Frequency (THz)')
ylabel('|Y(f)| (a.u)')
title('Comparision')
```

```
dx=f(3)-f(2);
tr = linspace(f(1),1/1/dx/(1-1/L),NFFT);
tr = timeps;
normnew=abs(Y2(1:NFFT/2));
normn = normnew.^2;
meandirac = mean(normn);
nn = sqrt(meandirac);
new1 = ifft(nn*(Y./Y2),NFFT)*L;
figure(7)
plot(tr,new1,'Linewidth',2), grid on
title('Reproduced Time-Domain Spectrum')
xlabel('Time (ps)')
ylabel('Amplitude (V)')
```

APPENDIX B

PREPULSE EFFECTS IN THz-TDS

In this section, we present the detection characteristics of two THz-TDS systems using both electro-optic and photoconductive detection. One of the THz-TDS is driven by a sub 15 fs pulsed Ti:Sapphire laser, the other is driven by a 150 fs pulsed Erbium-doped fiber laser as shown in Figure A.1. We observed pre-pulse effects in both electro-optic sampling and photoconductive antenna with both of the spectrometer systems. While the pre-pulse effects in the THz scan are due to gate reflections during electro-optic sampling, the effects observed with photoconductive antenna are not clear and need explanation.

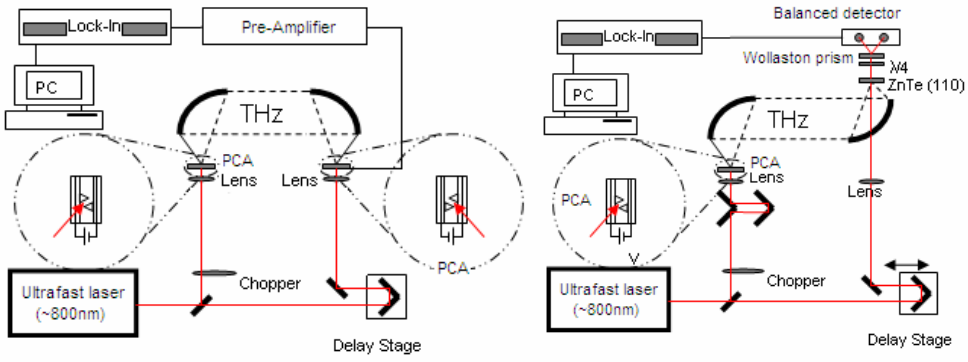

Fig.B.1. The THz-TDS on the left driven by Erbium-doped fiber laser, the one on the right is driven by Ti:Sapphire laser

In the experiments we have observed pre-pulses for three different configurations as seen in Figures A.2 and A.3 below.

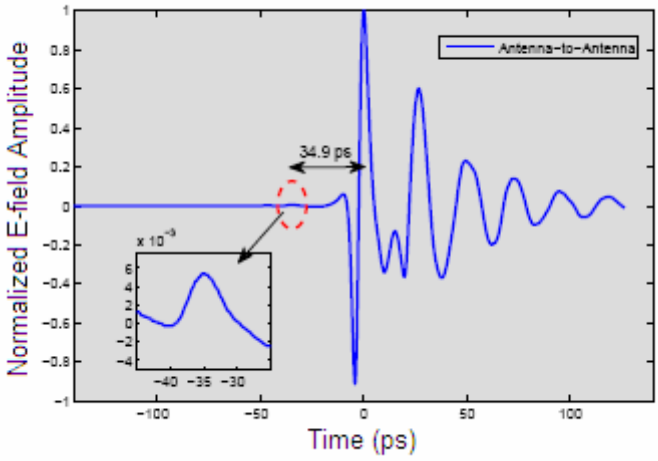

Fig.B.2. THz profile is shown for the photoconductive antenna generation and photoconductive antenna detection.

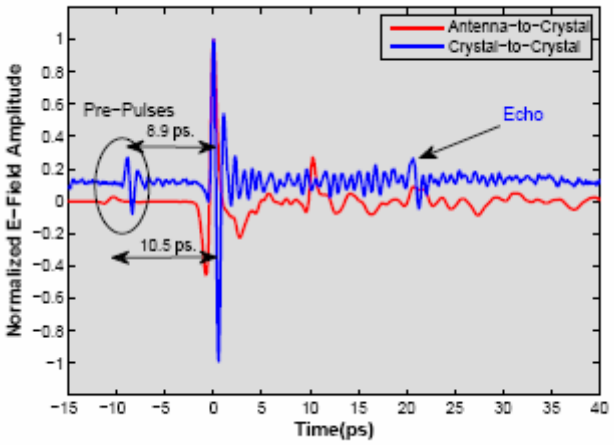

Fig.B.3. The graph shows both antenna generation and crystal detection (red) and electro-optic generation and electro-optic detection profiles.

These pre-pulses come earlier than the main pulses which are 8.9 ps for crystal to crystal (c-to-c), 10.5 ps for antenna-to-crystal (a-to-c) and 34.9 ps for antenna-to-antenna (a-to-a) configurations. The difference for the (c-to-c) and (a-to-c) configurations comes from the fact that THz pulse in c-to-c is narrower than that of (a-to-c). In order to explain pre-pulses which appear 34.9 ps earlier,

we need to get insight of physical mechanism that lies under that phenomenon. For now, however, it can be said that it is due gate reflections in the detecting antenna or due to more exotic processes like pre-pulse generation at the transmitter, the THz pulse has distortions which need to be accounted for during THz measurements.

While the prepulse arises from gate reflection at the crystal detector for electro-optic methods, the pre-pulse occurring in photoconductive detection is not clear and needs to be better understood.

VITA

Devrim Köseoğlu was born in Kırklareli. He got his B.S., M.S., and PhD. degrees from Middle East Technical University, Department of Physics. His research interests include Terahertz Science and Technology, Condensed Matter Physics, Photonics, Lasers and Optical system design.

Publications:

1. "*THz Probe Studies of MBE Grown Epitaxial GaAs*" {Electron Dynamics in Semiconductors, Optoelectronics and Nanostructures, Journal of Physics: JPCS, **193**, 012088 (2009)}

2. "*Numerical Improvement of Terahertz Time-Domain Spectroscopic Measurements*" {Proceedings of TERA-MIR 2009: NATO Advanced Research Workshop on Terahertz and Mid-Infrared Radiation: Basic Research & Practical Applications, November 2009}